Interfaces haptiques pour l'interaction physique humain-robot : Analyse et mise en oeuvre de l'approche macro-mini

Thèse

Jonathan Beaudoin

Doctorat en génie mécanique
Philosophiæ doctor (Ph. D.)

Québec, Canada

© Jonathan Beaudoin, 2022

Interfaces haptiques pour l'interaction physique humain-robot: Analyse et mise en oeuvre de l'approche macro-mini

Thèse

Jonathan Beaudoin

Sous la direction de:

Clément Gosselin, directeur de recherche

Résumé

Cette thèse présente la conception d'une interface haptique capable de rendre l'interaction physique humain-robot naturelle et intuitive. Il s'agit là d'un sujet d'étude très important avec l'avènement de la robotique collaborative et la présence toujours accrue des robots dans la vie de tous les jours. Les travaux présentés se concentrent sur l'approche macro-mini à titre d'interface haptique, plus particulièrement trois aspects importants lors de la conception d'un système macro-mini.

Le premier chapitre permet d'apprendre à *parler* physiquement au robot (lui faire comprendre les intentions de l'humain) dans un contexte de déplacement collaboratif. Plus particulièrement, il consiste à comparer différentes méthodes pour traduire les déplacements (ou les intentions) de l'humain à un robot. Dans ce cas, des coquilles à faible impédance sont attachées sur les membrures d'un manipulateur sériel. L'humain interagit avec le robot en déplaçant ces coquilles. La réponse du robot est alors de se déplacer de façon à ce que ses membrures suivent les déplacements de la coquille qui leur est associée pour ainsi les conserver dans leur configuration neutre.

Le déplacement d'une coquille par rapport à sa membrure est considéré comme une vitesse désirée de ladite membrure. Il s'agit donc de résoudre le problème cinématique inverse pour traduire le déplacement de la coquille en déplacement articulaire. Cependant, différentes stratégies peuvent être employées pour résoudre ce problème. Ce projet vise donc à comparer l'efficacité de ces méthodes.

Pour y parvenir, une étude générale de ces méthodes est réalisée. Puis, un formalisme mathématique est décrit pour adapter ces méthodes à l'application présente. En effet, en fonction du type de coquille et de la membrure, tous les degrés de liberté ne sont pas nécessairement possibles. Ce formalisme mathématique permet de tenir compte de ces contraintes. Ensuite, des simulations sont réalisées pour observer le comportement des méthodes étudiées et un indice de performance est choisi pour les comparer.

Ensuite, une fois que le robot est en mesure de comprendre efficacement les intentions humaines, le problème de conception consiste à déterminer comment détecter ses intentions à l'aide d'une interface et surtout, la taille que cette interface doit prendre pour bien *parler*.

En d'autres mots, le second chapitre présente une analyse de l'impact du débattement d'un mécanisme mini actif sur la bande passante mécanique de mouvements possibles lors de la manipulation de charges lourdes.

En effet, l'approche macro-mini utilise généralement un robot mini passif, ce qui fait que l'utilisateur ressent toute l'inertie de la charge. Lorsque la charge devient suffisamment lourde, il est nécessaire pour le mini d'appuyer l'utilisateur en fournissant une force pour conserver l'interaction naturelle. Ceci signifie que le mini doit être actionné, *i.e.*, actif. Il est cependant important que le mini reste rétrocommandable pour le bon fonctionnement de l'approche macro-mini.

Des modèles mathématiques du système sont donc présentés. Les contraintes relatives à l'application sont décrites ainsi que leur impact sur la bande passante. À l'aide d'un contrôleur simple, des simulations sont réalisées à l'aide des outils développés pour déterminer le débattement nécessaire du mini actif qui permet la bande passante désirée.

Enfin, une interface haptique capable de reproduire une poignée de main naturelle et intuitive avec un robot est présentée. Ce chapitre peut être divisé en deux aspects, *i.e.*, la main et le bras. Ici, la main est le robot mini et le bras, le robot macro.

D'abord, un prototype de main robotique est conçu et fabriqué. Inspirée de l'anatomie humaine, cette main robotique possède une paume comprimable capable d'émuler celle de l'humain ainsi que trois doigts sous-actionnés. Un pouce passif, relié au niveau de compression de la paume, complète le tout. Le contrôle de la main se fait via une position avec rétroaction, et ce, pour chacun des deux actionneurs (un pour la paume, l'autre pour les trois doigts).

Ensuite, la main robotique est montée sur un manipulateur sériel collaboratif (le *Kuka LWR*), le bras. Ce dernier est contrôlé en impédance autour d'une trajectoire harmonique dans un plan vertical. En fonction des paramètres de la trajectoire (amplitude, fréquence, coefficients d'amortissement et de raideur), ce prototype permet de conférer une personnalité active au robot. L'expérimentation faite auprès de sujets humains permet de déterminer les valeurs considérées plus naturelles pour les différents paramètres de la trajectoire ainsi que diverses pistes à explorer pour des travaux futurs.

Abstract

This thesis presents the design of a haptic interface capable of rendering a physical human-robot interaction natural and intuitive. It is a very important subject to study with the rise in collaborative robots and the ever-increasing presence of robots in everyday life. The work presented here focuses on the macro-mini architecture as haptic interface, more precisely on three important aspects to consider during the design of a macro-mini system.

The first chapter explores how to physically *communicate* with a robot (make it understand the human's intentions) in a context of collaborative motion. In more details, the goal is to compare different methods to translate human motions (or intentions) to a robot. In this case, low impedance passive articulated shells are mounted on the links of a serial manipulator. The human operator interacts with the robot by displacing the shells. The robot's response is then to move so that its links follow the motion of their associated shell. The better the robot can follow the shells, the closest to their neutral configuration the shells can remain.

The shell displacement relative to its link is considered as a desired velocity of the link. The translation of the shell displacement into joint motion then becomes an inverse kinematic problem. Different strategies can be used to solve this problem. This project then aims at comparing the efficiency of those strategies.

To this end, a general study of the different strategies is performed. Then, a mathematical formalism is described, adapting said strategies to the present context. Indeed, depending on the type of shell and the position of the link in the chain, all degrees of freedom are not necessarily possible. This formalism takes these limitations into account. Then, simulations are conducted to observe the behaviour of the different strategies studied and a performance index is chosen to compare them.

Afterwards, once the robot is capable of efficiently understanding the human intentions, the next step is to determine how to detect the intentions with the help of an interface and, most of all, what size should this interface have so as to *communicate* well. In other words, the second chapter presents an analysis of the impact that the range of motion of an active mini mechanism has on the mechanical bandwidth for the possible motions during the handling of large payloads.

Indeed, the macro-mini architecture generally uses a passive mini robot, which means that the human operator feels the whole inertia of the payload. When the payload becomes sufficiently heavy, it becomes necessary for the mini robot to help the operator by working as well so as to keep the interaction natural. This means that the mini robot should then be actuated, *i.e.*, active. It is however important that the mini robot remains backdrivable for the macro-mini architecture to work properly.

Mathematical models are then presented. The limitations related to the application are described, as well as their effect on the bandwidth. With the help of a simple controller, simulations are performed with the tools developed to determine the range of motion necessary for the active mini robot which would allow the desired bandwidth.

Finally, a haptic interface capable of emulating a natural and intuitive handshake with a robot is presented. This chapter can be divided into two aspects, *i.e.*, the hand and the arm. Here, the hand is the mini robot and the arm, the macro robot.

First, a robotic hand prototype is designed and constructed. Inspired by the human anatomy, this robotic hand has a compliant palm able to emulate a human palm as well as three underactuated fingers. A passive thumb, tied to the palm compression level, completes the hand. The hand control is done with position control with feedback for both actuators (one for the palm, the other for the three fingers).

Then, the robotic hand is mounted on a collaborative serial manipulator (the *Kuka LWR*), the arm. The arm is controlled in impedance around a harmonic trajectory in a vertical plane. Depending on the parameters for the trajectory (amplitude, frequency, stiffness and damping coefficients), this prototype provides an active personality to the robot. Experimentation is conducted with human subjects to determine the values considered more natural for the different trajectory parameters as well as several improvements for the prototype in future works.

Table des matières

Liste des tableaux

Liste des figures

À mes parents,

À ma famille,
Héritée comme choisie,

À ma dulcinée,

Mais surtout à moi-même,
Qui a toujours rêvé de robots.

Tout le monde voit ce que vous semblez être, peu de gens savent réellement qui vous êtes.

Niccolò Machiavelli, Le Prince

Remerciements

Je ne pourrais commencer autrement qu'en remerciant ceux qui m'ont donné la vie, mes parents. Ils m'ont logé et nourri tout au long de mes études, sans trop se plaindre. Ils ont toujours su appuyer mes intérêts et mes passions. Ils m'ont supporté lorsque j'en avais besoin et m'ont laissé à mes desseins, à mon indépendance le reste du temps, même si je vivais sous leur toit. Tout ceci n'aurait pu être possible avec des parents moindres. Merci infiniment, pour tout ce que vous avez fait pour moi et tout ce que vous ferez encore dans le futur. Merci également à ma soeur et mon frère qui m'ont enduré pendant tout ça.

Merci à Jean-Philippe, qui a su piquer ma curiosité dans tous les partys de famille avec ses histoires de maîtrise en robotique, tant d'années auparavant, et la naissance de son entreprise. Il y a quelques années, il m'y a fait une petite place, une place pour laquelle je serai éternellement reconnaissant. J'ai toujours aimé les robots, ça n'a fait que confirmer que je voulais y passer ma vie. Plus encore, Jean-Philippe m'a présenté celui qui deviendrait mon directeur de recherche.

Évidemment, je ne pourrais rédiger cette thèse sans mentionner Clément, mon directeur de recherche. Vos conseils et vos commentaires m'ont été d'une aide indispensable. Même si je ne suis pas très demandant (je crois), vous étiez toujours disponible quand j'en avais besoin, toujours capable de répondre à mes questions de votre savoir apparemment infini. J'espère que tous mes brouillons à réviser n'ont pas trop pesé sur vos épaules. À ce point, vous savez que je suis un homme de peu de mots. Vous avez su guider mon esprit vagabond à bon port. Alors, je me contenterai de ceci : merci énormément pour tout. Je ne l'oublierai jamais.

Pendant que j'y suis, j'aimerais également remercier tous les autres enseignant(e)s et professeur(e)s qui ont cru en moi et qui m'ont insufflé le désir de continuer. Je ne suis sans doute pas le meilleur élève et nombre de fois (si ce n'était pas toutes les fois) ai-je dû avoir l'air de ne pas écouter ou porter attention en cours. Merci d'avoir su capturer mon intérêt et mon imagination, même si ce n'était pas pendant les heures de classe.

Un grand merci également à Thierry et Simon. Vous étiez toujours présent pour moi quand j'avais besoin de vous, pour régler tous mes petits (ou gros) problèmes, tout au long de ma recherche. C'est très apprécié.

Pour tous ceux et celles qui, fois après fois, n'ont cessé de s'exclamer : «tu n'as pas encore fini tes

études ! ? »Chaque fois, dans les nombreuses dernières années, j'ai dû répondre : «pas encore, peut-être un jour. »Je peux enfin changer mon discours et répondre que j'y suis presque ! La fin est en vue ! Du moins, cette fois, je le crois.

Finalement, je tiens à remercier ma dulcinée, Véronique, qui a su redonner un sens à tous ces efforts, à un moment il n'y en avait plus vraiment. Je n'ai pas eu la chance de t'avoir à mes côtés très longtemps dans ce parcours, mais la qualité trône sur la quantité, dit-on. Je suis humblement comblé et content de t'avoir trouvée. Le meilleur nous est à venir, je le crois profondément et je ne l'échangerais pour rien au monde.

Avant-propos

La thèse ci-dessous présentée prends la forme d'une thèse par articles. Il est donc de mon devoir de préciser le statut des articles, à la date de soumission de la thèse, tout comme ma contribution à chacun d'eux. Pour faciliter la lecture, les informations relatives à chaque chapitre, *i.e.*, chaque article, sont données en points de forme.

Chapitre 1

Titre : Inverse Kinematics Strategies for Physical Human-Robot Interaction Using Low-Impedance Passive Link Shells

Type d'article : Article de journal, Robotica

Statut : Soumis, 2 décembre 2021

Contribution : Auteur principal. Rédaction, conception logicielle et simulation faites par l'auteur principal.

Coauteurs : Prof. Clément Gosselin a supervisé activement la réalisation et la finalité de cet article. Thierry Laliberté a conçu les coquilles et fait les expérimentations. Clément Gosselin et Thierry Laliberté ont développé le modèle mathématique pour adapter la cinématique inverse aux coquilles.

Chapitre 2

Titre : Analysis and design of a macro-mini robotic system for physical human-robot interaction

Type d'article : Article de journal, Elsevier Mechatronics

Statut : Soumis, 9 décembre 2021

Contribution : Auteur principal. Rédaction, conception logicielle et simulation faites par l'auteur principal.

Coauteurs : Muhammad Abdallah de chez General Motors et Prof. Clément Gosselin ont supervisé activement la réalisation et la finalité de cet article, ainsi que tout le processus de conception. Thierry Laliberté a appuyé tout au long du projet.

Chapitre 3

Titre : Haptic Interface for Handshake Emulation

Type d'article : Article de journal, IEEE Robotics and Automation Letters

Statut : Publié, 25 juillet 2019

Contribution : Auteur principal. Rédaction, conception et expérimentation faites par l'auteur principal.

Coauteurs : Prof. Clément Gosselin a supervisé activement la réalisation et la finalité de cet article. Thierry Laliberté a participé et aidé à la réalisation du projet concerné.

Introduction

> Ce n'est pas le titre qui honore l'homme, mais l'homme qui honore le titre.
>
> Niccolò Machiavelli

Contexte

Depuis plusieurs années, les robots, quelle que soit leur forme, prennent une part toujours grandissante dans la société. Dernièrement, cette part mène graduellement l'humain à interagir davantage avec divers robots. Que ce soit un androïde de science-fiction, un travailleur partageant son espace de travail avec un robot ou encore un robot aspirateur nettoyant le plancher, les contacts avec un robot seront, dans un futur plus ou moins proche, inévitables. L'interaction entre un humain et un robot devient donc de plus en plus importante. C'est d'autant plus vrai avec l'arrivée des robots collaboratifs destinés à travailler en collaboration avec les humains.

Le monde de l'interaction humain-robot est vaste et les différents exemples d'interactions sont légion. Tenir une conversation avec une intelligence artificielle, la reconnaissance de gestes par un capteur visuel quelconque, les exosquelettes ou encore les portes automatiques sont tous des exemples d'interaction humain-robot, pour n'en nommer que quelques-uns. Tous ces exemples peuvent être regroupés sous différents types d'interactions, *e.g.*, sonores, visuelles, physiques ou autres. L'étude de chacun de ces types est intéressante en soi et a sa valeur dans le grand monde de la robotique. Dans le cadre de cette thèse, les interactions physiques humain-robot sont étudiées.

L'interaction physique humain-robot regroupe les interactions où un humain et un robot communiquent à l'aide de contacts physiques. L'humain touche au robot pour le manipuler et vice-versa. Cette communication physique entre le robot et l'humain se fait généralement à l'aide d'une interface haptique. Il s'agit d'un outil permettant le transfert d'information par le sens du toucher, entre l'humain et le robot.

Différentes méthodes sont utilisées dans la littérature pour réaliser cette interface haptique, chacune avec différents niveaux de succès en fonction de l'application visée. Ces méthodes incluent l'utilisation d'un capteur d'effort avec un contrôle en admittance, de moteurs rétrocommandables avec un contrôle en impédance ainsi que le déploiement de l'architecture macro-mini, parmi tant d'autres. Ces méthodes sont survolées dans les différents chapitres de cette thèse. Parmi ces méthodes, l'étude de cette thèse se concentre sur une méthode en particulier, *i.e.*, l'approche macro-mini.

L'architecture macro-mini consiste à ajouter un petit mécanisme à faible impédance mécanique (le mini robot) à un plus grand mécanisme à haute impédance mécanique (le macro robot). En d'autres mots, il s'agit de fixer un petit robot agile à l'effecteur d'un gros robot plus lent, mais robuste. L'idée derrière ce concept est simple : le mini robot permet les déplacements à plus haute fréquence, mais est limité dans son débattement alors que le macro robot permet les plus grands déplacements, mais à plus basse fréquence.

Objectif de recherche

L'objectif global de la recherche consiste à produire une interface haptique capable de rendre une interaction physique naturelle et intuitive entre un humain et un robot. Il s'agit là d'un large défi pouvant être interprété de différentes façons. En effet, produire une interface haptique naturelle et intuitive est plutôt général comme objectif. D'abord, comment définit-on le caractère intuitif ou le naturel d'une interaction ? Puis, comment traduire ce caractère intuitif et ce naturel en comportement du robot ?

Pour la première question, la réponse simple qui vient à l'esprit est que le robot devrait se comporter comme un humain. Évidemment, un tel critère est difficile à quantifier et, pire encore, change sans doute d'une application à l'autre. En effet, l'humain possède une capacité d'adaptation que les robots n'ont simplement pas, ou du moins, pas au moment de l'écriture de cette thèse. Alors, comment quantifier le comportement humain d'un robot ?

Ensuite, en présumant être capable de répondre à cette première question, il faut être en mesure de rendre ce comportement humain à travers des moteurs, du métal ou toutes autres technologies actuelles. Si les technologies nécessaires n'existent pas, alors il faut les inventer, mais encore faut-il savoir ce dont on a besoin.

Ce sont là des questions bien difficiles à répondre sans grande connaissance *a priori*. Évidemment, la littérature a abondamment étudié ce sujet par le passé. Cette recherche s'ajoute donc à nombre d'autres qui ont tenté de trouver réponse à ces questions.

Plutôt que de répondre directement (et exactement) à ces questions, ce qui serait sans doute impossible, la recherche présentée ici se concentre sur des problèmes plus précis, mais toujours importants pour l'étude de l'interaction physique humain-robot en général. Ces problèmes

peuvent être vus comme des étapes franchies lors de ces travaux :

1. **Transmission de l'intention humaine au robot :** Une étude de différentes méthodes pour transmettre les mouvements de l'humain à un robot pour une application donnée utilisant l'architecture macro-mini comme interface.
2. **Analyse de la bande passante d'un système robotique pour l'interaction physique humain-robot :** Une analyse de l'impact de la taille du mécanisme mini sur la bande passante de l'interaction en fonction de différentes contraintes.
3. **Un type d'interaction physique humain-robot :** Un geste particulier d'interaction physique nécessitant une bonne bande passante est choisi dans le but de le reproduire avec un robot.

Plan de la thèse

Comme mentionné précédemment, la recherche est divisée en trois étapes distinctes, définie par les trois articles qui composent cette thèse.

La recherche de l'étudiant porte d'abord sur le guidage manuel d'un manipulateur sériel à l'aide de coquilles à faible impédance attachées aux membrures du manipulateur. En d'autres mots, l'utilisateur humain interagit avec les coquilles. Le robot réagit pour suivre le déplacement prescrit aux coquilles par l'utilisateur. Il s'agit d'une architecture macro-mini où le robot mini (les coquilles) est fixé sur une membrure du robot macro, plutôt qu'à son effecteur. Dans ce système, le robot macro est actif, c'est-à-dire qu'il est actionné, alors que le robot mini est passif.

La conception de ces coquilles a été réalisée au Laboratoire de Robotique de l'Université Laval dans le cadre de travaux antérieurs, alors que la recherche présentée ici se concentre principalement sur leur contrôle. Le but devient alors de déterminer l'efficacité de différentes méthodes pour traduire l'intention humaine en déplacement du robot par voie de simulations. Un indice quantitatif est utilisé pour comparer les différentes méthodes étudiées.

Le Chapitre 1 porte sur l'étude des différentes méthodes pour résoudre le problème cinématique inverse ainsi que sur leur application avec les coquilles. Plus particulièrement, ce chapitre se concentre sur la méthode de la pseudo-inverse amortie, de la Jacobienne transposée ainsi que la décomposition en valeurs singulières avec amortissement variable.

Ensuite, l'approche macro-mini repose sur la capacité de l'humain à déplacer le robot mini à l'aide d'une force raisonnable, *i.e.*, le robot mini est rétrocommandable. Pour cette raison, le robot mini est généralement passif. L'inconvénient d'un robot mini passif est son inaptitude à aider l'opérateur dans sa tâche. Cette inaptitude se fait particulièrement sentir lorsque la charge s'alourdit et l'opérateur doit ressentir toute l'inertie de la charge à déplacer.

La recherche présentée ici se concentre alors sur l'étude d'un mécanisme mini actif pour la manipulation de charges lourdes (de l'ordre de 100 kg). Un des principaux enjeux à considérer ici est la nécessité de conserver le robot mini rétrocommandable tout en étant capable de déployer suffisamment de force pour soutenir la majorité d'une charge lourde. L'objectif des travaux est de déterminer le débattement nécessaire au robot mini actif pour que le système ne limite pas la bande passante de l'interaction en considérant différentes contraintes prescrites, que ce soit des contraintes techniques, mécaniques, ergonomiques, de sécurité ou autres.

Le Chapitre 2 décrit cette étude d'un système macro actif/mini actif.

Finalement, un exemple bien précis d'interaction physique est choisi pour tenter de la reproduire avec un robot. Le type d'interaction choisi ici n'est nul autre que la poignée de main. Avant la pandémie, il s'agissait d'un geste facilement reconnaissable par presque toute culture sur la planète. La poignée de main représente un acte où les deux participants sont actifs, travaillant en tandem pour transmettre un message de confiance, de salutations, d'entente, ou autre.

Pour cette raison, la poignée de main représente un type d'interaction physique parfait pour l'étude du sujet. En effet, reproduire une poignée de main avec un robot peut sembler futile, à première vue. Cependant, comme la poignée de main est un geste des plus courant (hormis en période de pandémie), il est facile pour un sujet d'en juger le naturel, *i.e.*, de déterminer si le robot produit un comportement *humain*.

La poignée de main est un acte qui nécessite une bonne bande passante. Pour la réaliser, deux aspects sont importants : la main (paume et doigts) et le mouvement de cette main dans l'espace (le rôle du bras). Dans ce contexte, le robot mini est la main alors que le bras est le robot macro.

Plus encore, d'un point de vue de conception, il s'agit d'un dispositif relativement léger qui permet de faire l'expérimentation de façon raisonnablement simple et sécuritaire. L'étude de la poignée de main avec un robot est couverte dans le Chapitre 3.

Chapitre 1

Inverse Kinematics Strategies for Physical Human-Robot Interaction Using Low-Impedance Passive Link Shells

1.1 Résumé

Cet article présente une étude sur l'efficacité de différentes stratégies pour résoudre le problème cinématique inverse dans un contexte d'interaction physique humain robot. Plus particulièrement, ces stratégies sont employées en conjonction avec des coquilles passives articulées attachées aux membrures d'un manipulateur sériel pour un guidage manuel. Le concept des coquilles passives est d'abord évoqué. Puis, les stratégies pour résoudre le problème cinématique inverse sont décrites. Un manipulateur sériel à 5-dof utilisé dans des travaux antérieurs est brièvement présenté. Le robot est muni de deux coquilles passives destinées à l'interaction. Des résultats de simulations basés sur les différentes stratégies pour résoudre le problème cinématique inverse sont ensuite présentés, puis comparés. Finalement, des observations et des recommandations sont abordées.

1.2 Abstract

This paper presents an investigation of the effectiveness of different inverse kinematics strategies in a context of physical human-robot interaction in which passive articulated shells are mounted on the links of a serial robot for manual guidance. The concept of passive link shells is first recalled. Then, inverse kinematics strategies are presented and formulated. A serial 5-dof robot used in previous work is briefly introduced. The robot includes two link shells for interaction. Simulation results based on the different inverse kinematic strategies are then

presented and compared. Finally, general observations and recommendations are discussed.

1.3 Introduction

Industrial applications in which human workers and robots share a common workspace are nowadays common in industry. In the past years, numerous studies have touched on the advancements of robots that are safe enough to assist humans, whether it be in industry or at home. Different safety metrics and safety-related issues are introduced in [4]. A survey of the different forms of human-machine cooperation in assembly is presented in [5], which explores different safety systems as well. In [6], the development of a collaborative human-robot manufacturing cell compatible with the safety standards is described. A systematic evaluation of safety in human-robot interaction, covering the most significant injury mechanisms is proposed in [7]. If they are to fulfil their purpose, these robots should not only be safe, but also simple and intuitive to use.

Different approaches are studied throughout the literature to safely control a manipulator for the application of physical human-robot interaction (pHRI). In most cases, a rigid manipulator is controlled through an admittance control scheme. In [8], a velocity based variable impedance control using the differentiation of the force to infer human intention is presented. Reference [9] presents a variable admittance control approach to improve system intuitiveness, using desired velocity and acceleration for the inference of human intentions. In [10], a variable admittance control to deliver an optimal bilateral force amplification is introduced while a new variable admittance control law that guarantees the stability of the robot is proposed in [11]. Admittance control requires the use of a force/torque sensor to read the user's inputs and infer their intentions. The main drawback of this approach is that it introduces lag and delays, thereby affecting the intuitiveness of the interaction.

Alternatively, the macro-mini architecture overcomes this limitation by mounting a low-impedance mechanism (mini robot) at the rigid robot's end-effector. This method is first presented in [12; 13]. Reference [1] builds upon this concept and introduces a novel low-impedance mini mechanism specifically designed for physical human-robot cooperation. The uMan is presented in [3]. It consists of an underactuated manipulator designed with a novel passive mini mechanism, minimizing impedance. In reference [14], the mini mechanism is built upon the tripteron architecture [15] to eliminate parasitic motions. The macro-mini architecture can be used for different applications. For instance, references [16; 17] present a macro-mini robot designed for polishing and deburring using force control. In this approach, the user interacts only with the low-impedance mechanism, decoupling the robot's high impedance from the task. The mini mechanism's motion from its reference configuration relative to the end-effector dictates the robot's motion. However, in the case of a passive mini mechanism, since the payload is attached to the mini mechanism, the user feels its whole inertia, hindering

the interaction for large payloads.

Rather than placing the mini mechanism at the robot's end-effector, reference [18] proposes to mount a six-degree-of-freedom (6-dof) low-impedance passive shell on the robot's last link, thereby decoupling the task from both the structure of the robot and the payload. In reference [2], the 6-dof passive shell is replaced by two 3-dof shells mounted on two distinct links to make the interaction more intuitive.

The motion of the shells relative to the links is measured using encoders included in the mechanisms connecting the shells to the links. This motion is then used to infer the intentions of the human user. In references [18] and [2], the shell's motion is interpreted as desired link velocities. The inverse kinematics corresponding to the link on which a given shell is mounted is then solved to obtain the joint velocities. Nevertheless, different strategies can be employed to solve this problem. In order to study the impact of the different strategies and select the most appropriate approaches, this paper compares the behaviour of different inverse kinematics strategies when used with low-impedance passive link shells.

This paper is then structured as follows. First, the objective of the study is clearly stated. Second, a review of existing inverse kinematics strategies is briefly presented. Then, the serial manipulator and the low-impedance passive link shells used in this study are introduced. Next, the inverse kinematics strategies are adapted to the current objective and simulation results are provided. Finally, the results are analyzed and discussed to provide insightful recommendations.

1.4 Objective

As mentioned above, in reference [18], a low-impedance 6-dof passive link shell was designed to capture a human user's interaction commands and decouple the user's motions from the high-impedance structure of the robot in order to yield more natural physical human-robot interactions. The shell is mounted on the last link of a custom-built 5-dof serial manipulator to evaluate its performances. Reference [18] uses the damped least square pseudo-inverse method to solve the inverse kinematics.

In reference [2], the low-impedance 6-dof passive link shell is replaced by two redesigned 3-dof low-impedance passive link shells. The two shells are mounted on the third and fifth link of the same 5-dof serial manipulator.

The work introduced in this paper builds upon and expands the results presented in references [18] and [2]. In [2], a general formulation was presented that can be used to handle an arbitrary number of link shells placed along any of the links of a serial robot. Such an approach allows a user to control the motion of a robot by manipulating any of the links that are equipped with shells.

In this context, the objective of this paper is to study different strategies for the inverse kinematics based on the input provided by a human user, *i.e.*, based on a measured motion of the link shells. In other words, this paper addresses the issue of interpretation of the motion of the link shells to produce the motion of the robot that will most closely correspond to the intentions of the user. The strategies investigated are then applied to the arrangement presented in [2], namely, a 5-dof robot with two low-impedance passive link shells mounted on the third and fifth links, in order to compare their effectiveness.

1.5 Inverse Kinematics and Trajectory Planning of Serial Robots

In physical human-robot interaction, a user moves a robot from its current position rather than following a prescribed Cartesian trajectory. The robot's instantaneous motion, and hence its velocity, is then more relevant than its absolute position and orientation. The velocities of the end-effector are obtained from the joint velocities through the Jacobian matrix, as

$$\boldsymbol{t} = \boldsymbol{J}(\boldsymbol{\theta})\dot{\boldsymbol{\theta}} \tag{1.1}$$

where $\boldsymbol{t}$ is the six-dimensional end-effector velocity vector, $\dot{\boldsymbol{\theta}}$ is the joint velocity vector and $\boldsymbol{J}$ is the Jacobian matrix. The velocity vector $\boldsymbol{t}$ is defined by

$$\boldsymbol{t} = \begin{bmatrix} \boldsymbol{\omega} \\ \dot{\boldsymbol{p}} \end{bmatrix} \tag{1.2}$$

where $\boldsymbol{\omega}$ and $\dot{\boldsymbol{p}}$ are respectively the angular velocity vector and the velocity of the reference point on the end-effector. Given eq. 1.2, the Jacobian matrix can be written as

$$\boldsymbol{J}(\boldsymbol{\theta}) = \begin{bmatrix} \boldsymbol{A}(\boldsymbol{\theta}) \\ \boldsymbol{B}(\boldsymbol{\theta}) \end{bmatrix} \tag{1.3}$$

where $\boldsymbol{A}$ and $\boldsymbol{B}$ are the matrices related to the rotational and translational components, respectively.

Most likely, the desired trajectory is defined in the Cartesian space rather than in the joint space. Particularly, the approach described here interprets the inputs from link shells as Cartesian velocities of their associated links. The inverse problem must then be solved to yield the joint velocities from the desired end-effector velocity, namely

$$\dot{\boldsymbol{\theta}} = \boldsymbol{J}^I \boldsymbol{t} \tag{1.4}$$

where $\boldsymbol{J}^I$ is a generalized inverse and where the Jacobian's dependence on the joint coordinates is dropped for convenience. Several methods can be used to solve the inverse kinematics, depending on the context. The most common methods are now briefly reviewed.

1.5.1 Inverse Jacobian

If the Jacobian matrix is square and non-singular, then one can write

$$\boldsymbol{J}^I = \boldsymbol{J}^{-1}. \tag{1.5}$$

However, in a context of physical human-robot interaction, this solution can be applied only to special cases. Indeed, the inverse kinematics must be solved for a link of the robot on which a shell is mounted. In general, the degree of freedom of the link is different from the number of joints between the base of the robot and the link. In this case, the Jacobian matrix is therefore not square. Also, it is desired that the user be able to control the robot even when it is close to singular configurations.

The above considerations make this solution not generally applicable to pHRI robots in which the human user can apply motions to different links, which is the case in this work.

1.5.2 Pseudo-Inverse Jacobian

If the Jacobian matrix is not square but of full rank, the inverse problem can be solved by taking the pseudo-inverse rather than simply the inverse of the matrix. The pseudo-inverse solution is also known as the *Moore-Penrose* [19] inverse, noted $\boldsymbol{J}^\dagger$. One then has

$$\boldsymbol{J}^I \equiv \boldsymbol{J}^\dagger. \tag{1.6}$$

For a full-rank matrix, the *Moore-Penrose* generalized inverse yields the least-square solution for an overdetermined system, namely

$$\boldsymbol{J}^\dagger = (\boldsymbol{J}^T\boldsymbol{J})^{-1}\boldsymbol{J}^T, \tag{1.7}$$

meaning here that there are more degrees of freedom at the point of application of the inverse kinematics than there are joints between the base of the robot and the point of application.

For a full-rank underdetermined system of equations, the *Moore-Penrose* generalized inverse corresponds to the minimum norm solution, namely

$$\boldsymbol{J}^\dagger = \boldsymbol{J}^T(\boldsymbol{J}\boldsymbol{J}^T)^{-1}, \tag{1.8}$$

meaning here that there are more joints between the base and the point of application of the inverse kinematics than there are degrees of freedom at the point of application.

In the case of an overdetermined system, eq. 1.7 yields the Cartesian velocity vector that is as close as possible (in the sense of the least squares) to the prescribed Cartesian velocity vector.

In the case of an underdetermined system, equation 1.8 yields the solution with the smallest norm for the joint velocity vector that produces the prescribed Cartesian velocity vector.

The pseudo-inverse method provides a solution for non-square Jacobian matrices, but requires nonetheless a matrix inversion. The problem of a rank-deficient matrix remains.

1.5.3 Damped Pseudo-Inverse Jacobian

As mentioned above, when the robot is in a singular configuration, the Jacobian matrix is not of full rank. This means that a matrix inversion is not possible. However, this problem is not unconquerable.

In order to avoid the inversion of a matrix which is not of full rank, one can modify the matrix to make it invertible while slightly altering the solution. This method was first used in [20; 21]. For instance, considering eq. 1.7, the damped pseudo-inverse can be written as

$$\boldsymbol{J}^{\dagger} = (\boldsymbol{J}^T\boldsymbol{J} + \lambda^2\boldsymbol{I})^{-1}\boldsymbol{J}^T \tag{1.9}$$

where λ is the damping coefficient and $\boldsymbol{I}$, the identity matrix.

Using this approach, a solution that does not exactly meet the required Cartesian velocities is obtained. Nevertheless, it can be shown that by choosing an appropriate damping coefficient, a solution suitable for the application can be obtained.

1.5.4 Transpose Jacobian

Another possible approach to solve the inverse kinematic problem is to consider the robot as a quasi-static system and to assume that the desired speed at the point of application of the inverse kinematic is in fact a virtual force. Then, the resulting moment at the joints can be found from the transpose of the Jacobian matrix [22; 23]. In other words, the generalized inverse is taken as

$$\boldsymbol{J}^I \equiv \alpha\boldsymbol{J}^T \tag{1.10}$$

and equation 1.4 becomes

$$\Delta\boldsymbol{\theta} = \alpha\boldsymbol{J}^T\boldsymbol{t} \tag{1.11}$$

where α is a scaling factor.

While this method does not require a matrix inversion, it is not exactly equivalent either (hence the $\Delta\boldsymbol{\theta}$ notation rather than $\dot{\boldsymbol{\theta}}$). In order to determine the value of α that minimizes the error introduced by the use of eq. 1.10, it is first noted that $(\boldsymbol{J}\boldsymbol{J}^T\boldsymbol{t})^T\boldsymbol{t} \geq 0$ for all $\boldsymbol{J}$ and $\boldsymbol{t}$. Indeed, one has

$$(\boldsymbol{J}\boldsymbol{J}^T\boldsymbol{t})^T\boldsymbol{t} = (\boldsymbol{J}^T\boldsymbol{t})^T(\boldsymbol{J}^T\boldsymbol{t}) = \left\|\boldsymbol{J}^T\boldsymbol{t}\right\|^2 \geq 0. \tag{1.12}$$

If the angles $\Delta\boldsymbol{\theta}$ are changed by a sufficiently small $\alpha \geq 0$, then the end effector position should change by $\boldsymbol{t} \approx \alpha\boldsymbol{J}\boldsymbol{J}^T\boldsymbol{t}$. The value of α that minimizes the error between $\boldsymbol{t}$ and $\alpha\boldsymbol{J}\boldsymbol{J}^T\boldsymbol{t}$ is then obtained by

$$\alpha = \frac{\boldsymbol{t}^T(\boldsymbol{J}\boldsymbol{J}^T\boldsymbol{t})}{(\boldsymbol{J}\boldsymbol{J}^T\boldsymbol{t})^T(\boldsymbol{J}\boldsymbol{J}^T\boldsymbol{t})}. \tag{1.13}$$

1.5.5 Singular Value Decomposition

An alternative method to compute the pseudo-inverse of a matrix is the singular value decomposition. If $\boldsymbol{J}$ is the Jacobian matrix, then its singular value decomposition can be written as [24]

$$\boldsymbol{J} = \boldsymbol{U}\boldsymbol{D}\boldsymbol{V}^T \tag{1.14}$$

where $\boldsymbol{U}$ and $\boldsymbol{V}$ are orthogonal matrices and $\boldsymbol{D}$ is a diagonal matrix containing the singular values, σ_i. The rank r of $\boldsymbol{J}$ is equal to the number of non-zero singular values.

The singular value decomposition of $\boldsymbol{J}$ can be rewritten as

$$\boldsymbol{J} = \sum_{i=1}^{r} \sigma_i \boldsymbol{u}_i \boldsymbol{v}_i^T \tag{1.15}$$

where $\boldsymbol{u}_i$ and $\boldsymbol{v}_i$ are the i-th columns of $\boldsymbol{U}$ and $\boldsymbol{V}$, respectively.

Substituting eq. 1.14 into eq. 1.7 or eq. 1.8, one obtains

$$\boldsymbol{J}^\dagger = \boldsymbol{V}\boldsymbol{D}^\dagger\boldsymbol{U}^T \tag{1.16}$$

where $\boldsymbol{D}^\dagger$ is the pseudo-inverse of $\boldsymbol{D}$ such that

$$d_{i,i}^\dagger = \begin{cases} 1/d_{i,i} & , d_{i,i} \neq 0 \\ 0 & , d_{i,i} = 0 \end{cases}. \tag{1.17}$$

Then, eq. 1.16 can be rewritten as

$$\boldsymbol{J}^\dagger = \sum_{i=1}^{r} \sigma_i^{-1} \boldsymbol{v}_i \boldsymbol{u}_i^T \tag{1.18}$$

This method requires the computation of the reciprocal of non-zero scalars only, but it requires a singular value decomposition.

When the robot is near a singularity, at least one of the singular values σ_i is close to zero, making the inversion near singularities unstable. Similarly to eq. 1.9, one can damp this behaviour by introducing a damping coefficient. eq. 1.18 then becomes

$$\boldsymbol{J}^\dagger = \sum_{i=1}^{r} \frac{\sigma_i}{\sigma_i^2 + \lambda^2} \boldsymbol{v}_i \boldsymbol{u}_i^T. \tag{1.19}$$

In the *selectively damped least squares* method [25], a different damping value is chosen for each singular value σ_i. The damping coefficients depend not only on the current configuration of the manipulator, but also on the distance between the end effector and the target position.

1.6 Serial Manipulator with Low-Impedance Passive Link Shells

As mentioned above, this paper aims at developing strategies to exploit the concept of low-impedance link shells proposed in [18] and [2]. The concept behind the low-impedance shell introduced in [18] and [15] is now briefly recalled.

The low-impedance shell draws from the macro-mini architecture [12; 13] in which a small (mini) robot is attached to a larger (macro) active robot to control the motion of the end-effector and allow a low-impedance interaction with a human user. The mini manipulator can be either active or passive. The goal of this architecture is to decouple the macro's impedance from the task and from the human user when used in a context of pHRI. In some cases, the mini manipulator also carries the payload [1; 3; 14]. Also, the mini robot can be passive, in which case the user feels the payload's impedance.

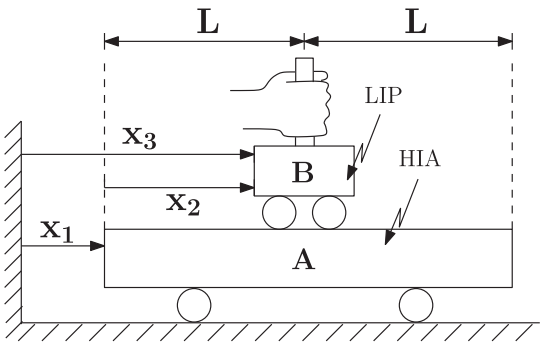

FIGURE 1.1 – Representation of the one-degree-of-freedom macro-mini manipulator, figure taken from [1].

The concept of the macro-mini architecture is explained in detail in [1; 3; 14; 18] and briefly recalled here for convenience. Fig. 1.1 illustrates a one-degree-of-freedom macro-mini manipulator for simplicity. The mini manipulator B is mounted on the macro manipulator A. The range of motion of the mini robot B, relative to the macro robot A, is given by $2L$. Its neutral position $x_2 = 0$ is determined, usually the centre of its reachable range, relative to the macro robot A. When the user manipulates the mini robot B away from its neutral position, the macro robot A moves in order to follow it. Therefore, the user indirectly guides the macro robot A throughout the workspace. The maximum speed and acceleration that the user can impart to the mini robot B depends on the ability of the macro robot A to catch up with the mini robot. The complete kinematic analysis is presented in [1; 3; 14; 18].

The principle of the macro-mini manipulators can be applied to a serial robot by mounting low-impedance shells around the links of the robot, as shown in Fig. 1.2 and described in [18] and [2]. The shell is a low-impedance passive mechanism mounted on the link of a serial

manipulator, rather than its end-effector. It is then decoupled from the structure of the robot and the payload. Although the shells are mounted on passive mechanisms, their joints are equipped with encoders so that the relative motion between the shells and the links can be measured. Given the robot's speed and desire to maintain the shell in its neutral configuration by following it, the user interaction is decoupled from the robot's impedance. The mechanism connecting the shell to the robot link includes preloaded springs and mechanical limits that tend to return the shell to a neutral configuration when no external forces are applied on it.

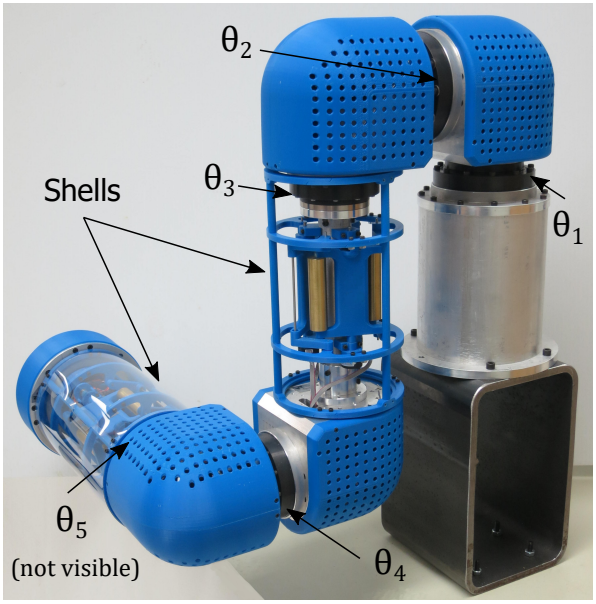

FIGURE 1.2 – Photograph of the experimental 5-dof robot with the low-impedance displacement sensors mounted on links 3 and 5, figure taken from [2].

For the purpose of this paper, the 5-dof serial manipulator introduced in [18] is used and its architecture is recalled here for convenience. The general architecture is presented in Fig. 1.2. The architecture is based on two clusters of joints : one with three motors near the base and the other with two motors near the end-effector.

When a single shell is used near the end-effector, the 6-dof shell developed in [18] works well. However, in such a case, only the last link of the robot can be manipulated by the human user. In order to enhance the interaction between a user and the robot, it is desirable to implement additional shells on the links of the robot closer to the base. Since these links have fewer degrees of freedom, using 6-dof shells becomes inefficient. Furthermore, the high number of input signals becomes more complicated to interpret.

For this reason, the 6-dof shell used in [18] is replaced by two 3-dof sensitive shells in [2]. The 3-dof shells are easier to balance and require lower pre-loads which means smaller and more intuitive interaction forces for the user. They also use revolute joints rather than prismatic joints. Instead of using a Gough-Stewart architecture, a planar 3-RRR parallel mechanism

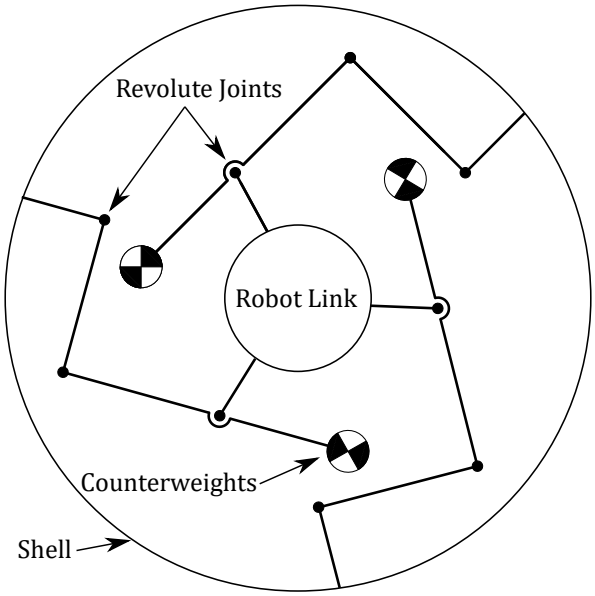

FIGURE 1.3 – Cross-section link and a 3 DOFs low-impedance link shell architecture, figure taken from [2].

is used, thereby providing two translational degrees of freedom in the directions orthogonal to the link axis and one rotational degree of freedom around the link axis, as illustrated in Fig. 1.3. All sensors are positioned at the base of the shell, which simplifies the wiring.

The shells are mounted respectively on the third and fifth links of the 5-dof serial manipulator. Each of the shells has two translational dofs in the plane perpendicular to the link axis and one rotational dof around the link axis.

1.7 Inverse Kinematics and Trajectory Planning Strategies

The different strategies presented in Section 1.5 are general approaches to solving the inverse kinematics problem at the velocity level. The objective of this research is to use these strategies in conjunction with the input motions measured between the shells and the links on which they are mounted. To this end, these general strategies must be adapted.

The mapping of the desired motion — measured by the encoders mounted on the shell mechanisms — onto the joint space of the robot is described in [2] and is briefly repeated here for convenience. Considering link i of the serial n-dof robot, one can write

$$\boldsymbol{t}_i = \boldsymbol{J}_i \dot{\boldsymbol{\theta}}_i \tag{1.20}$$

where $\boldsymbol{J}_i$ is the Jacobian matrix, with dimension $(6 \times i)$, of link i, $\dot{\boldsymbol{\theta}}_i$ is the vector containing the first i joint velocities and $\boldsymbol{t}_i$ is the vector of cartesian velocities of link i.

Consider a shell mounted on link i, which has ℓ_i dofs for the user inputs. The user input vector associated with shell i is noted $\boldsymbol{c}_i$ which contains ℓ_i components.

One can easily eliminate the rows of eq. 1.20 that do not have any component corresponding to the dofs of the shell, so as not to constrain them unnecessarily, by using a selection matrix $\boldsymbol{S}_i$. Matrix $\boldsymbol{S}_i$ is of dimension $(\ell_i \times 6)$. By expressing the Jacobian matrices in their respective link's space, $\boldsymbol{S}_i$ is defined as a matrix whose components are all zero except for ℓ_i unit components spread between the rows. The j-th component of each row is one if the j-th row of $\boldsymbol{J}_i$ is to be kept.

Using the selection matrix $\boldsymbol{S}_i$, eq. 1.20 is reduced to the relevant dofs as

$$\boldsymbol{S}_i \boldsymbol{t}_i = \boldsymbol{S}_i \boldsymbol{J}_i \dot{\boldsymbol{\theta}}_i \tag{1.21}$$

and, therefore, $\boldsymbol{S}_i \boldsymbol{J}_i$ is of dimension $(\ell_i \times i)$. The expression $\boldsymbol{S}_i \boldsymbol{t}_i$ is a function of $\boldsymbol{c}_i$.

In order to select which joints react to which shell, a reduction matrix $\boldsymbol{R}_i$ is introduced, of dimension $(i \times k_i)$ where $k_i \leq i$ is the number of joints that should be reacting to the shell of link i. Reduction matrix $\boldsymbol{R}_i$ is a matrix whose components are all zero except that each column has its j-th component equal to one if the j-th joint is active. Then, $\dot{\boldsymbol{\theta}}_{ir} = \boldsymbol{R}_i^T \dot{\boldsymbol{\theta}}_i$ contains only the active components of $\dot{\boldsymbol{\theta}}_i$. eq. 1.21 can be further reduced to

$$\boldsymbol{S}_i \boldsymbol{t}_i = \boldsymbol{S}_i \boldsymbol{J}_i \boldsymbol{R}_i \boldsymbol{R}_i^T \dot{\boldsymbol{\theta}}_i \tag{1.22}$$

or

$$\boldsymbol{t}_{is} = \boldsymbol{W}_i \dot{\boldsymbol{\theta}}_{ir} \tag{1.23}$$

where $\boldsymbol{W}_i = \boldsymbol{S}_i \boldsymbol{J}_i \boldsymbol{R}_i$ is the selected and reduced Jacobian matrix and $\boldsymbol{t}_{is} = \boldsymbol{S}_i \boldsymbol{t}_i$.

Eq. 1.3 shows that the Jacobian matrix can be partitioned into two submatrices, $\boldsymbol{A}$ and $\boldsymbol{B}$, the first for the rotational velocities and the second for the translational velocities. Since both submatrices use different units and different scales, the selected and reduced Jacobian should be partitioned, as

$$\boldsymbol{W}_i = \begin{bmatrix} \boldsymbol{W}_{ir} \\ \boldsymbol{W}_{it} \end{bmatrix} \tag{1.24}$$

where $\boldsymbol{W}_{ir}$ corresponds to the rotations and $\boldsymbol{W}_{it}$, to the translations. Vector $\boldsymbol{t}_{is}$ is partitioned as well to yield

$$\boldsymbol{t}_{isr} = \boldsymbol{W}_{ir} \dot{\boldsymbol{\theta}}_{irr} \tag{1.25}$$

$$\boldsymbol{t}_{ist} = \boldsymbol{W}_{it} \dot{\boldsymbol{\theta}}_{irt} \tag{1.26}$$

where $\boldsymbol{t}_{isr}$ represents the rotational components of $\boldsymbol{t}_{is}$ and $\boldsymbol{t}_{ist}$, the translational components.

Finally,

$$\dot{\boldsymbol{\theta}}_{ir} = \dot{\boldsymbol{\theta}}_{irr} + \dot{\boldsymbol{\theta}}_{irt} \tag{1.27}$$

which is equivalent to considering shell i as two distinct sensors, one for the rotations and the other for the translations.

In order to solve eq. 1.25 and 1.26 for the joint velocities, $\boldsymbol{W}_{ir}$ and $\boldsymbol{W}_{it}$ must be inverted. These matrices may not be square, which means that the simple matrix inverse (Section 1.5.1) cannot be used in this context. Also, the method should be applicable in singular configurations, which rules out the straightforward use of the pseudo-inverse method (Section 1.5.2). Therefore, the damped pseudo-inverse (Section 1.5.3) is used.

For the singular value decomposition (Section 1.5.5), a different approach can be used. Since this method treats all singular values individually, different options are presented. One can choose to damp all of them as in eq. 1.19, whether or not they are near a singularity (meaning the singular value is close enough to zero). On the other hand, one can also decide to damp only those near singularities or even not to consider them at all, *i.e.*, equating their contribution to zero in the summation of eq. 1.18, since the robot should not be able to move in the singular desired direction.

1.7.1 Direct Rotations

The architecture of the custom-built serial manipulator used in this work is such that the rotational input of the shells is aligned with their respective joint axis. Therefore, one could map the rotational input directly to the current joint only with a proportional function and the two translational inputs to the preceding joints using one of the aforementioned methods. Mathematically, this method could be written as

$$\dot{\boldsymbol{\theta}}_{ir} = \eta r_i \boldsymbol{e}_i + \dot{\boldsymbol{\theta}}_{irt} \tag{1.28}$$

where η is simply a scaling factor, r_i is the rotational input and $\boldsymbol{e}_i$ is a vector whose components are all zero except for the i-th component which is equal to one. In this case, $\boldsymbol{t}_i$ becomes a two-component vector of the translational inputs.

1.8 Simulation and Comparison of the Trajectory Planning Schemes

To summarize, the method proposed in [2] — and summarized in Section 1.7 — to map the inputs from the link shells onto a serial manipulator joint velocities can be implemented using any of the five approaches described in Section 1.5. Of these approaches, this paper studies the effectiveness of the Damped Pseudo-Inverse (Section 1.5.3), the Jacobian transpose (Section 1.5.4) and the Singular Value Decomposition (Section 1.5.5) inverse kinematics strategies in order to assess their capability to provide an intuitive response to the user inputs. To this end, simulation results based on an assumed input trajectory are presented in this section.

i	a_i [m]	b_i [m]	α_i [rad]	θ_i [rad]
1	0	0.2905	$\pi/2$	θ_1
2	0	0.1885	$\pi/2$	θ_2
3	0	0.3835	$\pi/2$	θ_3
4	0	0.1745	$\pi/2$	θ_4
5	0	0.1900	$\pi/2$	θ_5

TABLE 1.1 – DH parameters of the 5-DOF serial manipulator.

It can be shown that eqs. 1.9 and 1.19 yield the same results. Indeed, the singular value decomposition is just another algorithm to compute the general solution of a linear system of equations. For this reason, comparing the simple damped singular value decomposition grants no additional information. Rather, a variable damping coefficient λ^2 is used in 1.19, given by

$$\lambda_i^2 = \begin{cases} -\lambda^2(3\sigma_i^2 - 2\sigma_i^3) - \lambda^2 & , \sigma_i < 1 \\ 0 & , \sigma_i \geq 1 \end{cases} \tag{1.29}$$

where λ represents the maximum damping coefficient when $\sigma_i = 0$.

1.8.1 Robot Parameters

The robot parameters used for the simulation correspond to the serial manipulator developed in [18], as given in Tables 1.1 and 1.2.

j	$\dot{\boldsymbol{\theta}}_{j,max}$ [rad/s]	$\ddot{\boldsymbol{\theta}}_{j,max}$ [rad/s^2]
1	$4\pi/3$	22
2	$4\pi/3$	22
3	$4\pi/3$	54
4	$4\pi/3$	54
5	2π	60

TABLE 1.2 – Maximum speed and acceleration for the robot's joints.

1.8.2 Trajectory

A trajectory for the low-impedance shell is needed to compare the different strategies studied. However, since the robot's response may differ depending on the strategy used, it is not possible to specify a shell trajectory in the fixed reference frame. Moreover, the shell's location in space is constrained by the link's pose and cannot be prescribed arbitrarily. For these reasons, determining a Cartesian shell trajectory *a priori* is difficult. A quasi-Cartesian trajectory is used instead, as described here. The procedure is illustrated in Fig. 1.4 considering a 1-dof shell for simplicity.

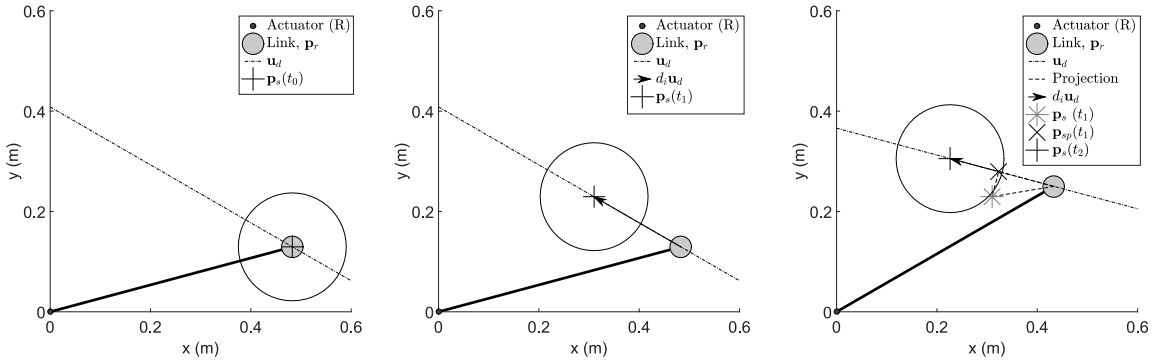

(a) Time $t_0 = 0$. (b) Time $t_1 = t_0 + \Delta t$. (c) Time $t_2 = t_1 + \Delta t$.

FIGURE 1.4 – Schematic representation of the shell trajectory for a 1-dof shell mounted on a link.

First, a general harmonic motion is determined, given by

$$d = D\sin(2\pi f t) \tag{1.30}$$

as well as a feasible direction of motion $\boldsymbol{u}_d$, expressed in the link's space. For instance, $\boldsymbol{u}_d$ must be in the plane perpendicular to the link's axis for the 3-dof shell presented earlier. For the 1-dof example, $\boldsymbol{u}_d$ is defined by the only possible direction of motion, shown by the dotted line in Fig. 1.4.

At $t_0 = 0$, the shell is at rest, meaning it is at the origin of the link's coordinate system located in the neutral configuration.

$$\boldsymbol{p}_s(t_0) = \boldsymbol{p}_{ref}(t_0). \tag{1.31}$$

At $t_1 = t_0 + \Delta t$, where Δt is given by the sampling frequency, the shell is moved in the desired direction a distance $d_1 = d(t_1) - d(t_0)$ based on the harmonic function given in eq. 1.30

$$\boldsymbol{p}_s(t_1) = \boldsymbol{p}_s(t_0) + d_1\boldsymbol{Q}_l\boldsymbol{u}_d \tag{1.32}$$

where the matrix $\boldsymbol{Q}_l$ is used to express $\boldsymbol{u}_d$ in the Cartesian space, rather than the link space. The robot moves according to the method chosen for solving the inverse kinematics.

At $t_2 = t_1 + \Delta t$, the shell might not be in a feasible location relative to its associated link due to the reaction of the robot. The shell position is then projected onto its feasible space to simulate its compliance to the constraints imposed by its architecture during motion. For example, Fig. 1.4c shows that $\boldsymbol{p}_s(t_1)$ is no longer on the dotted line representing its feasible locations. However, it should be kept on this line during motion, hence the projection $\boldsymbol{p}_{sp}(t_1)$. Then, the shell is moved once more in the desired direction a distance $d_2 = d(t_2) - d(t_1)$

$$\boldsymbol{p}_s(t_2) = \boldsymbol{p}_{sp}(t_1) + d_2\boldsymbol{Q}_l\boldsymbol{u}_d \tag{1.33}$$

and the cycle starts anew.

The maximum range of the shell relative to the link is verified for each time step, $\|[\boldsymbol{p}_s(t_i)]_l\| \leq p_{max}$, where $[\boldsymbol{p}_s(t_i)]_l$ represents the shell's position relative to its link and p_{max} is the maximum range of motion of the shell. The joints' acceleration and speed are also limited to the values given in Table 1.2 and $\lambda^2 = 0.1$ is used for each of the methods using a damping coefficient.

1.8.3 Results

In order to compare the different methods for solving the inverse kinematics, the angle ψ between the link's Cartesian velocity and the shell's motion is studied. Indeed, a smaller angle ψ means that the robot better follows the user's inputs.

As previously mentioned, two low-impedance shells are attached to the robot, mounted on the third and fifth links. Since the architecture of the joint upstream from the shell, relative to the shell, is the same for both shells, one can study the motion of either one. The shell on the third link is chosen here.

The results obtained vary depending on the direction of $\boldsymbol{u}_d$ relative to the robot's configuration. For this reason, a direction referred to as *optimal* is chosen. The initial configuration is chosen as the one shown in Fig. 1.2 and $\boldsymbol{u}_d$ is parallel to the fifth link, in this configuration. This direction is called *optimal* for two reasons. First, a force in this direction would produce a pure moment around the second joint's axis, regardless of the robot's configuration. Second, the same force would produce a pure moment around the first joint's axis for the robot's initial configuration. Choosing such a direction should yield $\psi = 0$ in the initial configuration, *i.e.*, the direction of motion coincides with the motion of the shell, hence the optimal direction.

Three trajectories are studied. The parameters of eq. 1.30 are given in Table 1.3 for each of the trajectories. Trajectory 1 represents a normal trajectory where both the robot and the

Trajectory	D [mm]	f [Hz]
1	100	1
2	500	1
3	100	3

TABLE 1.3 – Trajectory parameters.

shell remain within their limits. This means that the joints do not reach their maximum speed and the shell does not reach its physical limits.

Trajectories 2 and 3 represent trajectories where both the robot and the shell reach their limits. The former uses a high amplitude while the latter uses a high frequency to achieve this.

The results obtained for angle ψ, *i.e.*, the angle between the direction of motion of the shell

and the link, are presented in Figs. 1.5, 1.6 and 1.7 for the three trajectories and the three methods for inverse kinematics.

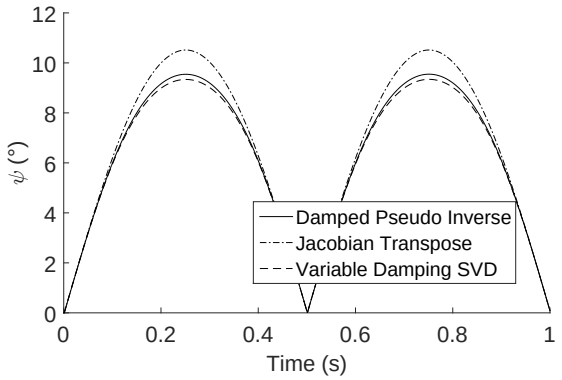

FIGURE 1.5 – Trajectory 1 : angle ψ between link speed and shell speed.

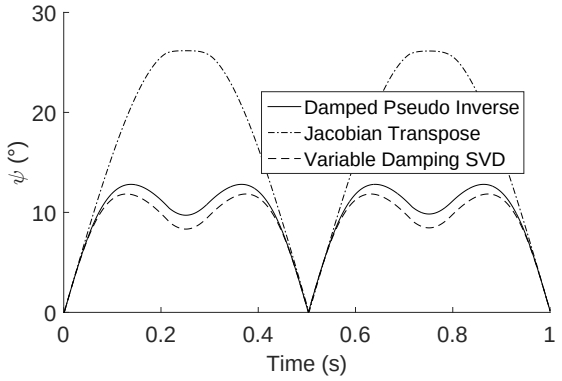

FIGURE 1.6 – Trajectory 2 : angle ψ between link speed and shell speed.

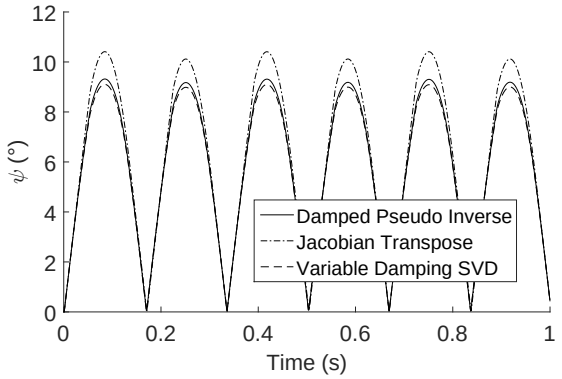

FIGURE 1.7 – Trajectory 3 : angle ψ between link speed and shell speed.

The results show little difference (a few degrees) between using the damped pseudo-inverse

Jacobian strategy and the singular value decomposition using a variable damping coefficient, as expected. For all three figures, the angles ψ for the Jacobian transpose method are larger than those for the other two strategies, only a few degrees for Figs. 1.5 and 1.7, and about double for Fig. 1.6.

Figs. 1.5 and 1.7 illustrate similar results if the difference in frequency is omitted. Fig. 1.6 shows a different behaviour. This implies that the robot's configuration is more important than the frequency f, for the present application. The higher the amplitude D is, the farther from its initial configuration the robot moves.

Fig. 1.6 illustrates two different phenomena, mainly the large values of angle ψ for the Jacobian transpose strategy and the angle oscillation near the change of direction of the movement for the other two methods. Both can be explained similarly.

As previously mentioned, Fig. 1.2 shows the robot's initial configuration. Link 3 is parallel to link 1. The joint axes are aligned with their respective link. Vector $\boldsymbol{u}_d$ is in the direction of link 5. When the shell on link 3 is moved, joints 1 and 2 move according to the right-hand rule. As the position of joint 2 (θ_2) increases, $\boldsymbol{u}_d$ aligns itself more and more with the axis of joint 1. In other words, when θ_2 has moved by 90°, $\boldsymbol{u}_d$ is parallel to link 1. This means that at this point, joint 1 can only produce a motion of the link that is perpendicular to $\boldsymbol{u}_d$, a purely parasitic motion. The Jacobian would be singular for this particular direction and configuration. The robot could then be reduced to one dof when considering link 3. Only joint 2 would be active at this point.

During the motion, θ_2 increases and the angle between $\boldsymbol{u}_d$ and link 1 decreases, which means that the parasitic nature of the motion of joint 1 increases. The Jacobian matrix accounts for this and reduces the involvement of joint 1. At some point, the reduced motion of joint 1 equates and then overcompensates its parasitic motion. Then, the system approaches the one-dof robot mentioned earlier. If θ_2 were to reach 90°, the angles shown in Fig. 1.6 would drop back to zero. They would then rise again as θ_2 moves away from 90°, which explains the oscillation.

This phenomenon is also visible for the Jacobian transpose strategy, although much less drastically. The point at which the reduced motion of joint 1 equates the parasitic link motion it induces happens at a higher value of θ_1. This point is closer to the change in direction of the trajectory, which decreases greatly the oscillations. This means that joint 1 moves more than for the other two strategies, incurring a larger parasitic motion. Hence, the angles between the link's Cartesian velocity and the shell's Cartesian motion are larger.

The results show that the Jacobian transpose strategy yields larger values of angle ψ for all three figures. Fig. 1.6 shows a maximum value of angle ψ slightly over 25° where the other two strategies yield about 13°. Experimentation would be required to determine if a user can

perceive the difference of about 12° as the Jacobian transpose strategy confers other advantages which are non-negligible. The Jacobian transpose strategy does not require a matrix inversion and the oscillation of alignment are greatly reduced.

1.9 Conclusion and Future Work

As previously mentioned, this paper's objective is to quantitatively compare different strategies to solve the inverse kinematics when used in conjunction with the low-impedance sensitive shells developed in [18] and [2]. To this end, the different strategies are presented and then adapted to fit the current application. The manipulator and the low-impedance sensitive shell are described as well. Then, a simulation is conducted to compare quantitatively the different strategies.

Since the relative motion between the shell and its associated link is taken as the desired link Cartesian velocities, the instantaneous angle between the shell's motion and the link's velocity is studied. Also, since a Cartesian trajectory for the shell cannot be determined beforehand, a procedure is developed to generate such a trajectory while taking into account the architecture of the robot and the shells.

The results from the simulations show that the performances vary greatly depending on the robot's configuration and the direction of the shell's motion. Furthermore, the Jacobian transpose strategy tends to yield the worst results while the damped pseudo-inverse and the singular value decomposition achieve similar results, as expected. Nevertheless, the advantage that the Jacobian transpose grants by avoiding the matrix inversion is not to be dismissed.

In the future, experimentation should be conducted to assert whether a human user can discriminate between the different results obtained in the simulations. If it is not the case, then the Jacobian transpose strategy may be preferable to the other two because of its computational simplicity.

1.10 Financial Support

This work was supported by the Natural Sciences and Engineering Research Council of Canada (NSERC) and by the Canada Research Chair program.

Chapitre 2

Analysis and design of a macro-mini robotic system for physical human-robot interaction

2.1 Résumé

L'architecture macro-mini a été étudiée par le passé dans le but d'aider avec les interactions physiques humain-robot. Cet article se concentre sur l'étude d'un système macro actif/mini actif destiné à la manipulation de charges lourdes. Plus particulièrement, une analyse du système est présentée dans le but de déterminer le débattement nécessaire pour le robot mini actif, en considérant différentes contraintes. Pour y parvenir, différents profils de déplacement sont d'abord comparés pour démontrer que l'utilisation de déplacements harmoniques est appropriée. Puis, les modèles cinématique et dynamique du système sont décrits. Les différentes contraintes, telles que les normes de sécurité, les capacités cinématiques et dynamiques des deux robots (macro et mini), la force maximale force permise par l'humain et autres, et leur impact sur la bande passante de l'interaction sont énoncés. Un contrôleur simple utilisé pour les simulations est introduit. Finalement, les résultats de simulations sont présentés et le déphasage entre le robot macro et le robot mini est observé, pour un déplacement harmonique simple de la charge. En plus du déphasage, les modèles mathématiques décrits sont utilisés pour obtenir le comportement de l'amplitude du déplacement du robot mini en fonction de la fréquence. Pour les contraintes choisies (inspirées de valeurs réelles), il est démontré qu'en diminuant de moitié la vitesse maximale à laquelle la charge peut se déplacer (de $1\,\mathrm{m\,s^{-1}}$ à $0.5\,\mathrm{m\,s^{-1}}$) diminue le débattement nécessaire du robot mini par un facteur d'environ 4.

2.2 Abstract

The macro-mini architecture has been studied in the past to help with physical human-robot interaction. This paper focuses on the investigation of an active macro/active mini robotic system for the manipulation of large payloads. More precisely, an analysis of the system is presented with the goal of determining the range of motion necessary for the active mini robot, considering several limitations. To this end, different motion profiles are first compared to show that using harmonic motion is appropriate. Then, the kinematic and dynamic models of the system are described. The different limitations, such as safety standard, kinematic and dynamic capabilities of both robots (macro and mini), human maximum allowable force and others, and their impact on the interaction bandwidth are stated. A simple controller used for simulations is introduced. Finally, simulation results are presented and the phase shift between the macro robot and the mini robot is observed, for a simple harmonic motion of the payload. Along with the phase shift, the mathematical models derived are used to obtain the behaviour of the mini robot's amplitude as a function of frequency. For the chosen limitations (based on realistic values), it is shown that reducing the payload maximum allowed velocity by half (from $1\,\mathrm{m\,s^{-1}}$ to $0.5\,\mathrm{m\,s^{-1}}$) reduces the necessary motion range of the mini by a factor of approximately 4.

2.3 Introduction

The last several years have seen a significant increase in the use of robots. With the advances in new technologies, the automation of more and more applications becomes possible. However, some tasks still require the agility and/or adaptability of the human touch. Such tasks cannot be fully automated, but robots can still assist humans to make them easier and more efficient, thereby introducing the concept of physical human-robot interaction (pHRI).

When robots and humans share a common workspace, safety is of paramount importance. For this reason, several papers have explored robots that are safe enough to share a common space with humans, whether it be in industry or even at home. In [4], different safety metrics and safety-related issues are introduced. Reference [5] presents a survey of the different forms of human-machine cooperation in assembly and explores different safety systems. In [6], the development of a collaborative human-robot manufacturing cell compatible with the safety standards is described. A systematic evaluation of safety in human-robot interaction, covering the most significant injury mechanisms is proposed in [7].

In addition to ensuring safety, a robot designed for pHRI must provide intuitive interactions. Here, intuitiveness can refer to a variety of concepts, depending on the task to be accomplished. Physical human-robot interaction, where a human being and a robot physically collaborate to achieve a goal, represents an important category of tasks in industry. This is evidenced by the advent of collaborative robots in the last few years [26].

In this particular case, an intuitive behaviour means a behaviour that corresponds to simple dynamics, *i.e.*, impedances that are linear, continuous and decoupled. So the question arises : how to sense and interpret the human interactions so that the robot can react accordingly ? The literature presents a variety of solutions to this question.

For one, admittance control has been used successfully in several applications. Admittance controllers use force/torque sensors to infer the human operator's intentions and produce a motion of the robot. In [8], a velocity based variable impedance control using the differentiation of the force to infer human intention is presented. Reference [9] presents a variable admittance control approach to improve system intuitiveness, using desired velocity and acceleration for the inference of human intentions. In [10], a variable admittance control to deliver an optimal bilateral force amplification is introduced while a new variable admittance control law that guarantees the stability of the robot is proposed in [11]. However, admittance control introduces a delay between the human force being applied and the reaction from the robot, *i.e.*, it limits the bandwidth of the physical human-robot interaction. For this reason, the intuitiveness of such a system is often limited or lacking.

Rather than reading a force to produce a motion, impedance control expects a motion input and outputs a force from the robot [27]. For this reason, force sensors can be omitted, requiring only position sensors. While this type of control is effective, it requires a robot with a low mechanical impedance. In other words, the robot needs to be backdrivable, so that the input force applied by the human operator can produce a motion of the actuators.

However, in applications where large payloads are manipulated, the forces required from the human operator may be too large and the implementation of impedance control then becomes impractical. A possible approach to address this issue is the macro-mini architecture. This method, first presented in [12; 13], introduces a low-impedance mechanism (mini) attached at the end-effector of the high-impedance robot (macro). Reference [1] builds upon this concept and introduces a novel low-impedance mini mechanism specifically designed for physical human-robot cooperation. The uMan, shown in Figs. 2.1 and 2.2, is presented in [3]. It consists of an underactuated manipulator designed with a novel passive mini mechanism, minimizing impedance. In reference [14], the mini mechanism is built upon the tripteron architecture [15] to eliminate parasitic motions. The macro-mini architecture can be used for different applications. For instance, references [16; 17] present a macro-mini robot designed for polishing and deburring using force control.

In this work, it is assumed that the human operator interacts with the payload and the mini mechanism, allowing low-impedance interaction. The controller interprets this motion and the macro reacts accordingly to follow the payload. Conceptually, the mini mechanism can be viewed as a force sensor where the deformations are of the order of centimetres (rather than micrometres as in force/torque sensors).

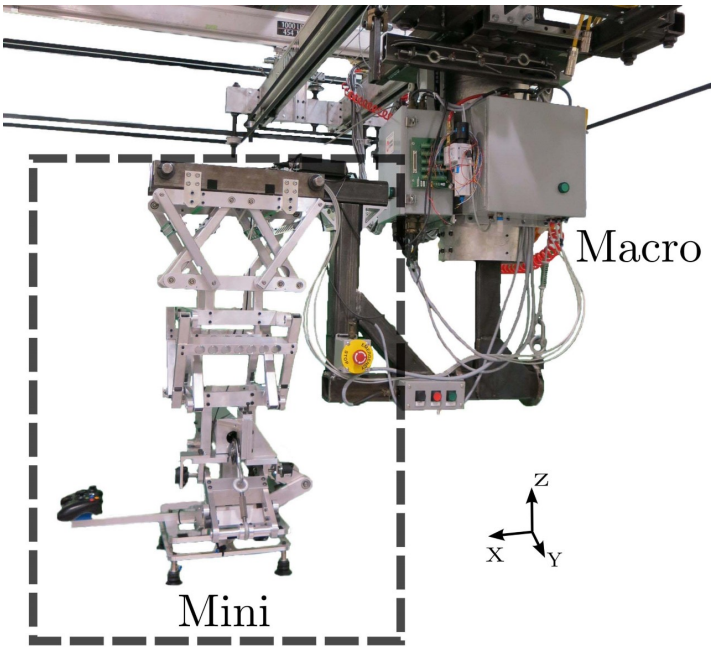

FIGURE 2.1 – The uMan, an active macro/passive mini robotic system for manufacturing applications (from [3]).

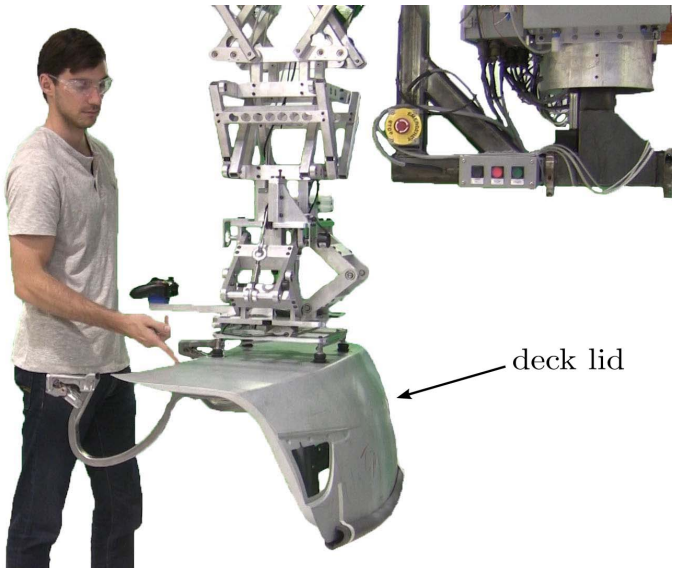

FIGURE 2.2 – Manipulation of a payload (a decklid) using the active macro/passive mini uMan system (from [3]).

In references [1; 3; 14], the use of a passive mini mechanism is successfully demonstrated. A passive mini mechanism provides a very intuitive and natural interface that yields high adaptability and precise control for the human operator. However, one drawback of a passive mini mechanism is that the inertia of the payload is felt by the human operator. For payloads of the order of 50 kg or less, this approach can be effective. However, for larger payloads, the

demands on the operator become too large and an active mini can help alleviate this issue.

This paper focuses on the investigation of an active macro/active mini robotic system. More precisely, the goal is to develop design guidelines to determine the range of motion required for the active mini in order to provide a given desired bandwidth for the physical human-robot interaction. The determination of the required range of motion of the mini robot is very critical in a design context. Indeed, a large range of motion (in other words, a large mini) reduces the motion demands on the less agile macro robot. On the other hand, it requires larger and stronger actuators, which means more weight added to the system. Therefore, a compromise must be reached between the size of the mini and the possible motion prescribed by the human operator (interaction bandwidth).

This paper is structured as follows. In Section 2.4, a comparison of different types of motion profiles is presented. Section 2.5 then introduces a kinematic model as well as a dynamic model of the system. These models are then used in Section 2.6 to assess the impact of the different physical limitations of the system, such as maximum velocity, acceleration, and others. A simple controller for the macro-mini system is then described in Section 2.7 to simulate the behaviour of the complete system. In Section 2.8, simulations are conducted, using realistic values for the different parameters. The simulation results are then used to assess the impact of the range of motion of the mini on the bandwidth of the physical human-robot interaction provided by the active macro/active mini system. It is shown that the models and simulations presented in this work can be used as guidelines for the design of an active macro/active mini robotic system. Finally, concluding remarks are made.

2.4 Comparison of the motion profiles

In most robotics applications, pick and place trajectories are dominant. Different methods can be used to plan a trajectory, from a point A to a point B. These methods impose different profiles for the velocity and acceleration of the actuators. Examples of such profiles are the 5th-degree polynomial [28] and the trapezoidal velocity profile [29; 30].

In order to study the bandwidth of a macro-mini system, a periodic motion between two points is prescribed at the end-effector. This periodic motion can be based on a harmonic oscillation, a fifth-order polynomial or a trapezoidal velocity profile, which can affect the results obtained. For this reason, this section compares the requirements of a harmonic motion with the other two methods in order to confirm the validity of using pure harmonic motion.

2.4.1 Harmonic Motion

A generic harmonic motion is illustrated in Fig. 2.3 and given as

$$x_H = A\sin(\omega t) \tag{2.1}$$

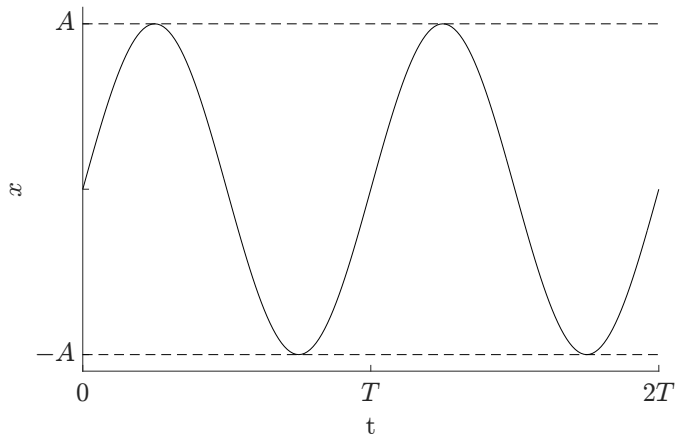

FIGURE 2.3 – Harmonic motion.

$$\dot{x}_H = A\omega\cos(\omega t) \tag{2.2}$$

$$\ddot{x}_H = -A\omega^2\sin(\omega t). \tag{2.3}$$

Since $\omega = 2\pi/T$, where T is the harmonic motion period, then the maximum velocity and maximum acceleration reached during this motion, noted $\dot{x}_{H,max}$ and $\ddot{x}_{H,max}$, are given by

$$\dot{x}_{H,max} = 2\pi\frac{A}{T} \approx 6.3\frac{A}{T} \tag{2.4}$$

$$\ddot{x}_{H,max} = 4\pi^2\frac{A}{T^2} \approx 39.5\frac{A}{T^2}. \tag{2.5}$$

2.4.2 5th-degree Polynomial

A trajectory based on a 5th-degree polynomial is illustrated in Fig. 2.4 and given by

$$x_{P5} = A_{P5}(6\tau^5 - 15\tau^4 + 10\tau^3). \tag{2.6}$$

In order to compare the polynomial to one peak to peak section of the harmonic motion, we select $\tau = 2t/T$ and $A_{P5} = 2A$. Then (2.6) and its derivatives become

$$x_{P5} = 2A(6\tau^5 - 15\tau^4 + 10\tau^3) \tag{2.7}$$

$$\dot{x}_{P5} = \frac{4A}{T}(30\tau^4 - 60\tau^3 + 30\tau^2) \tag{2.8}$$

$$\ddot{x}_{P5} = \frac{8A}{T^2}(120\tau^3 - 180\tau^2 + 60\tau). \tag{2.9}$$

The maximum velocity and maximum acceleration reached during this motion, noted $\dot{x}_{P5,max}$ and $\ddot{x}_{P5,max}$, are given by

$$\dot{x}_{P5,max} = \frac{15}{2}\frac{A}{T} = 7.5\frac{A}{T} \tag{2.10}$$

$$\ddot{x}_{P5,max} = \frac{80\sqrt{3}}{3}\frac{A}{T^2} \approx 46.2\frac{A}{T^2}. \tag{2.11}$$

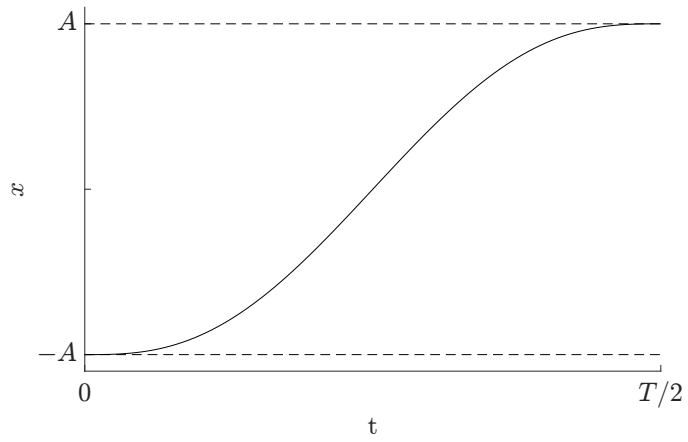

FIGURE 2.4 – 5th-degree polynomial trajectory.

2.4.3 Trapezoidal Velocity Profile

A trapezoidal velocity profile is illustrated in Fig. 2.5. By finding the area under the curve,

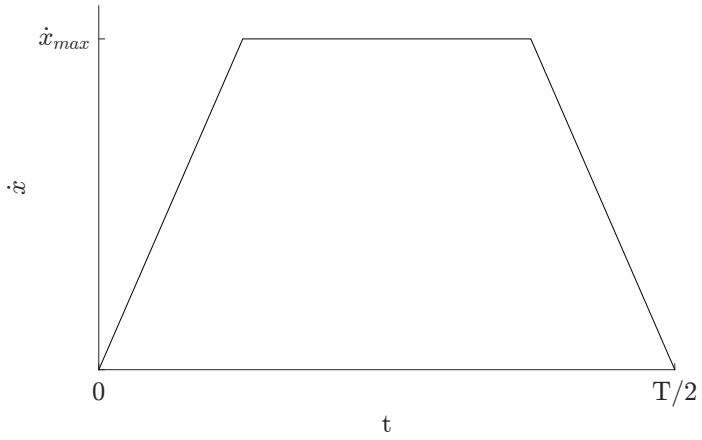

FIGURE 2.5 – Trapezoidal velocity profile.

and assuming symmetry (*i.e.*, the magnitude of the acceleration and of the deceleration are equal) for a total duration of the motion equal to $T/2$ and displacement amplitude $2A$, one has

$$2A = \dot{x}_{T,max}(t_{rise} + t_{const}) \tag{2.12}$$

$$t_{rise} = \frac{\dot{x}_{T,max}}{\ddot{x}_{T,max}} \tag{2.13}$$

$$t_{const} = \frac{T}{2} - 2\frac{\dot{x}_{T,max}}{\ddot{x}_{T,max}} \tag{2.14}$$

where $\dot{x}_{T,max}$ is the maximum velocity, t_{rise} is the duration of the acceleration phase of the motion, t_{const} is the duration of the constant velocity phase of the motion and $\ddot{x}_{T,max}$ is the magnitude of the acceleration in the rising phase. Then the maximum acceleration reached is given by

$$\ddot{x}_{T,max} = \frac{2\dot{x}_{T,max}^2}{T\dot{x}_{T,max} - 4A}. \tag{2.15}$$

If we set $\dot{x}_{T,max} = \dot{x}_{H,max}$ in (2.15), i.e., if the maximum velocity is assumed equal to the maximum velocity reached in the harmonic motion, then

$$\ddot{x}_{TH,max} = \frac{8\pi^2}{2\pi - 4}\frac{A}{T^2} \approx 34.6\frac{A}{T^2}. \tag{2.16}$$

Similarly, if we set $\dot{x}_{T,max} = \dot{x}_{P5,max}$ in (2.15), *i.e.*, if the maximum velocity is set to be equal to the maximum velocity reached in the harmonic motion, then

$$\ddot{x}_{TP5,max} = \frac{15^2}{7}\frac{A}{T^2} \approx 32.1\frac{A}{T^2}. \tag{2.17}$$

2.4.4 Interpretation

It can be observed that the values for the maximum velocity and the maximum acceleration obtained with each of the three velocity profiles are comparable. Since a harmonic motion is easier for the analysis, it is used throughout this study.

2.5 Kinematic and dynamic models

This section models the macro-mini system from both a kinematic and a dynamic standpoint. For simplicity, a one-dof translational motion is assumed, *i.e.*, a redundant system with a one-dof macro robot and a one-dof mini robot. The proposed model can be readily extended to multi-dof systems, including revolute or prismatic actuators.

2.5.1 Kinematic Model

In [1], a kinematic model for a 1-DoF macro-mini mechanism was introduced. This model is adapted here. Fig. 2.6 illustrates a 1-DoF macro-mini mechanism. x_1 denotes the position of the macro robot with respect to the base frame, x_2 denotes the position of the mini robot with respect to the macro robot, x_3 denotes the position of the mini robot with respect to the base frame and L represents the possible range of motion for the mini, *i.e.*, $|x_2| < L$. From Fig. 2.6, one has

$$x_2 = x_3 - x_1. \tag{2.18}$$

In order to evaluate the frequency response of such a system, as mentioned before, a simple harmonic motion is ascribed to the end-effector x_3. Therefore, the desired input motion can

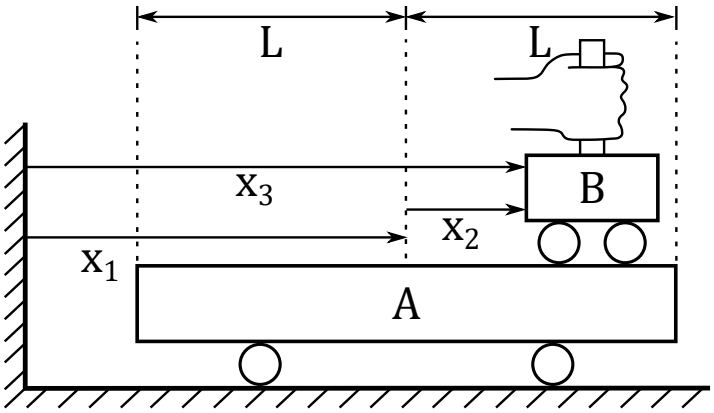

FIGURE 2.6 – Schematic representation of a 1-DOF macro-mini mechanism (adapted from [1]).

be expressed as

$$x_3 = A_3 \sin(\omega t). \tag{2.19}$$

The macro robot is programmed to follow the mini robot and maintain it within its range of motion. Accordingly, x_1 reacts proportionally to x_3 and in the same direction, assuming that the steady-state is achieved. Its motion is therefore expressed as a harmonic motion with the same frequency, namely

$$x_1 = A_1 \sin(\omega t + \phi) \tag{2.20}$$

where ϕ represents the phase delay between x_1 and x_3. Different reasons can cause this delay, *e.g.*, the time response of the control system, the communication or even the actuation, the different maximum accelerations reachable by both the mini and macro, and others.

From trigonometric identities, (2.19) and (2.20) can be substituted into (2.18) to find x_2, yielding

$$x_2 = A_2 \sin(\omega t + \gamma) \tag{2.21}$$

where

$$A_2 = \sqrt{A_3^2 + A_1^2 - 2A_3 A_1 \cos\phi}. \tag{2.22}$$

The expression for γ can be readily obtained but is not of much interest for the present study.

2.5.2 Dynamic Model

The free-body diagrams of the macro and mini mechanisms are shown in Fig. 2.7, where f_1 is the actuator force of the macro, f_2 is the actuator force of the mini and f_h is the force applied on the mini by the human user. Also, m_1 and m_2 represent respectively the moving mass of the macro and the mini. The control strategy described later on aims at reducing the payload mass felt by the user. To achieve this, the mini robot and the human user work together, *i.e.*, f_2 and f_h are in the same direction. The macro robot will be programmed to follow the mini

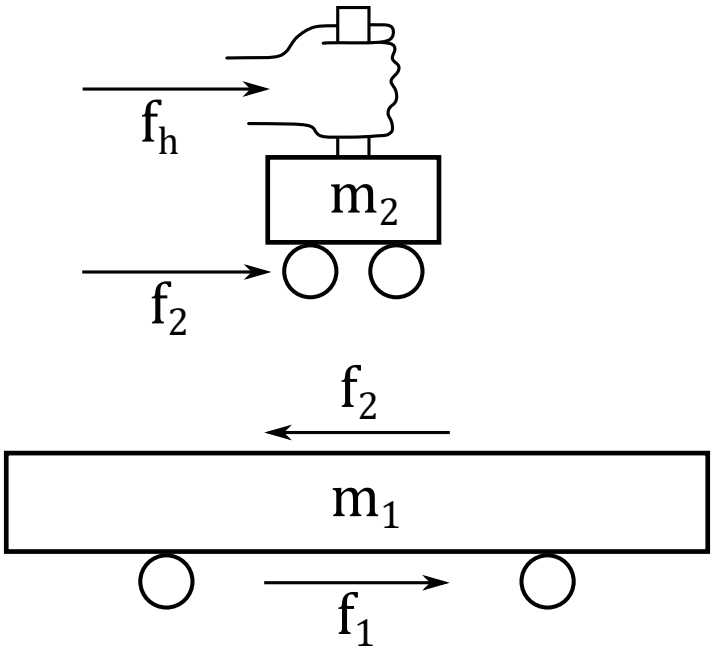

FIGURE 2.7 – Free body diagram of a 1-DOF macro-mini mechanism .

robot. Therefore, f_1 acts with f_h as well. Since the mini robot is mounted on the macro robot, its reactive force on the macro robot is in the inverse direction. Applying Newton's second law on each of the diagrams yields

$$f_h + f_2 = m_2(\ddot{x}_1 + \ddot{x}_2) = m_2\ddot{x}_3 \tag{2.23}$$

$$f_1 - f_2 = m_1\ddot{x}_1 \tag{2.24}$$

which are the two equations of motion of the system.

2.6 Impact of the kinematic and dynamic limitations on the interaction bandwidth

In order to ensure a smooth and natural experience to the human user, the mini should not reach its physical limits, *i.e.*, one must ensure that $|x_2| \leq L$. Referring to (2.21), one obtains

$$A_2 \leq L \tag{2.25}$$

where A_2 is defined in (2.22). Both the macro and the mini, as well as the overall system and application, have specific limitations. These limitations impose constraints on the motion that the system can achieve for a given range of motion of the mini. This section explores the impact of different limitations on the maximum achievable amplitude, for a given frequency and range of motion of the mini.

2.6.1 Kinematic Limitations

For simplicity, an ideal case is first assumed in which the macro and mini are perfectly synchronized. In this case, $\phi = 0$ and (2.22) becomes

$$A_2 = A_3 - A_1. \tag{2.26}$$

For an amplitude of input motion A_3 larger than L, the desired position is outside of the motion range of the mini mechanism. The macro must then move accordingly with a displacement of

$$A_1 = A_3 - L. \tag{2.27}$$

The velocity and the acceleration are given by the first and second time derivatives of (2.20), respectively, which yields

$$\dot{x}_1 = A_1\omega\cos(\omega t + \phi) \tag{2.28}$$

$$\ddot{x}_1 = -A_1\omega^2\sin(\omega t + \phi) \tag{2.29}$$

in which it is assumed that $\phi = 0$.

The velocity and acceleration limitations of the macro's actuator are noted $\dot{x}_{1,max}$ and $\ddot{x}_{1,max}$. The maximum reachable amplitude for the macro, for a given frequency, is then constrained by

$$A_{1,v} \leq \frac{\dot{x}_{1,max}}{\omega} \tag{2.30}$$

$$A_{1,a} \leq \frac{\ddot{x}_{1,max}}{\omega^2} \tag{2.31}$$

where $A_{1,v}$ and $A_{1,a}$ represent respectively the maximum reachable amplitude of x_1 given the velocity or acceleration limitations.

By rearranging (2.27) and substituting A_1 by $A_{1,v}$, the maximum amplitude of input motion x_3 with respect to frequency ω and the range of motion of the mini L [14] is obtained as

$$R_v \leq \frac{\dot{x}_{1,max}}{\omega} + L \tag{2.32}$$

where R_v stands for the maximum range of input motion that is feasible due to the velocity limitation.

Similarly, the relationship for R_a, the maximum range of input motion that is possible due to the acceleration limitation, is given by substituting A_1 in (2.27) by $A_{1,a}$ and solving for A_3 [14], yielding

$$R_a \leq \frac{\ddot{x}_{1,max}}{\omega^2} + L. \tag{2.33}$$

2.6.2 Dynamic Limitations

The macro and mini robots impose constraints on the maximum forces that can be produced. Also, the forces applied by the user should not exceed a threshold corresponding to ergonomic limitations. These constraints can be represented by the following inequalities

$$|f_h| \leq f_{h,max} \tag{2.34}$$

$$|f_1| \leq f_{1,max} \tag{2.35}$$

$$|f_2| \leq f_{2,max} \tag{2.36}$$

where $f_{h,max}$, $f_{1,max}$ and $f_{2,max}$ denote the maximum forces.

First, consider the limits that arise from the macro dynamics. From (2.24), (2.27) and (2.29), one can write

$$f_1 - f_2 = m_1 \ddot{x_1} = -m_1(A_3 - L)\omega^2 \sin(\omega t). \tag{2.37}$$

Assuming steady-state and zero phase, one gets, from the limitations on the macro mechanism

$$m_1(R_1 - L)\omega^2 \leq f_{1,max} - f_{2,max} \tag{2.38}$$

where R_1 is the maximum feasible range of input motion due to the force constraints on the macro side, which can be rearranged as

$$R_1 \leq \frac{f_{1,max} - f_{2,max}}{m_1\omega^2} + L. \tag{2.39}$$

Next, consider limits that arise from the mini dynamics. From (2.23) one can write

$$f_h + f_2 = m_2 \ddot{x_3} = -m_2 A_3 \omega^2 \sin(\omega t) \tag{2.40}$$

which leads to

$$m_2 A_3 \omega^2 \leq f_h + f_2 \tag{2.41}$$

and the limitations on the mini mechanism then yield, once again assuming steady state and zero phase,

$$m_2 R_2 \omega^2 \leq f_{max} = f_{h,max} + f_{2,max} \tag{2.42}$$

where R_2 is the maximum feasible range of input motion due to the force constraints of the mini and which can be expressed as

$$R_2 \leq \frac{f_{max}}{m_2\omega^2}. \tag{2.43}$$

As mentioned above, another limitation comes from the maximum force that a human user can effectively apply for a given period of time. Indeed, the objective of the active mini robot (as opposed to a passive mini robot) is to assist the human user and limit the force f_h that is

required to operate the system. With a given maximum force f_h from the user, the maximum amplitude that can be reached for a harmonic input motion is given by

$$f_{h,max} = m_r \ddot{x}_{3,max} = m_r A_3 \omega^2 \tag{2.44}$$

where m_r is the mass rendered to the user by the system, *i.e.*, the effective inertia felt by the user. The rendered mass m_r is a control parameter and its minimum value possible is given by the mini dynamics, namely

$$m_{r,min} = m_2 \frac{f_{h,max}}{f_{2,max} + f_{h,max}}. \tag{2.45}$$

Equation (2.44) can be rearranged as

$$R_h \leq \frac{f_{h,max}}{m_r \omega^2} \tag{2.46}$$

where R_h stands for the maximum range of motion that can be produced for a given maximum user force $f_{h,max}$ and a given rendered mass m_r and frequency ω. When $m_r = m_{r,min}$, (2.43) and (2.46) give the same results.

2.6.3 Other Limitations

Other limitations can impose constraints on the possible motion. For instance, safety standards limit the maximum velocity of the payload, $\dot{x}_{3,max}$. Then, a harmonic input motion with this maximum velocity must have an amplitude given by

$$R_s \leq \frac{\dot{x}_{3,max}}{\omega} \tag{2.47}$$

where R_s stands for the limitation corresponding to the velocity limit.

Equations (2.39), (2.43), (2.47) and (2.46) represent the dynamic limitations associated with the maximum forces and the maximum velocity constraint for safety.

2.7 Control

As mentioned before, the macro robot is programmed to follow the mini robot and keep the latter within its range of motion. In other words, the objective of the macro is to keep the mini as close as possible to its reference (mid-range) position. A simple controller designed to achieve this behaviour is presented here in order to assess the performance of the macro/mini system and study the impact of the different parameters. The dynamic model of the system was presented in Section 2.5, namely in (2.23) and (2.24), for which the Laplace transforms are given by

$$F_1 - F_2 = m_1 s^2 X_1 \tag{2.48}$$

and

$$F_h + F_2 = m_2 s^2 X_3 \tag{2.49}$$

where s is the Laplace variable and where F_1, F_2, F_h, X_1 and X_3 are the Laplace transforms of the corresponding lowercase variables.

2.7.1 Controller of the Macro Robot

The objective of the macro robot is to keep the mini robot as close as possible to its reference position, which means that $x_2 = x_3 - x_1$ should tend to zero. Therefore, the following control law is used for the macro

$$f_{1d} = k_{1p}(x_3 - x_1) + k_{1d}(\dot{x}_3 - \dot{x}_1) + f_{2d} \tag{2.50}$$

where f_{1d} is the desired force to be applied at the macro's actuator and k_{1p} and k_{1d} are proportional and derivative gains. The term f_{2d} is added to compensate for the active mini's force applied on the macro mechanism (see Fig. 2.7 and (2.24)).

In the Laplace domain, (2.50) becomes

$$F_{1d} = (k_{1p} + k_{1d}s)(X_3 - X_1) + F_{2d} \tag{2.51}$$

where F_{1d} and F_{2d} are the Laplace transforms of f_{1d} and f_{2d}.

To simplify the study of this controller, the force produced by the actuator is assumed to be the same as the desired force, namely

$$F_1 \simeq F_{1d}. \tag{2.52}$$

2.7.2 Controller of the Mini Robot

The desired behaviour for the mini robot is to render a prescribed virtual mass m_r and virtual damping c_r to the human user. Mathematically, this can be expressed as

$$f_h = m_r \ddot{x}_3 + c_r \dot{x}_3. \tag{2.53}$$

Substituting (2.53) into (2.23), the following is obtained

$$f_{2d} = (m_2 - m_r)\ddot{x}_3 - c_r \dot{x}_3 \tag{2.54}$$

and, in the Laplace domain

$$F_{2d} = [(m_2 - m_r)s^2 - c_r s]X_3. \tag{2.55}$$

Similarly to the macro robot, the force produced by the actuator is assumed to be the same as the desired force, for simplicity, *i.e.*,

$$F_2 \simeq F_{2d}. \tag{2.56}$$

2.7.3 Closed-Loop Behaviour of the Macro-Mini Robot

The system's closed-loop behaviour is obtained by substituting (2.52) and (2.56) into (2.48) and (2.49), which yields for the macro

$$X_1 = C_M X_3 \tag{2.57}$$

where

$$C_M = \frac{k_{1d}s + k_{1p}}{m_1 s^2 + k_{1d}s + k_{1p}} \tag{2.58}$$

and for the mini

$$X_3 = C_m F_h \tag{2.59}$$

where

$$C_m = \frac{1}{s(m_r s + c_r)} \tag{2.60}$$

2.7.4 Poles

From (2.58), the poles for the macro are given by

$$p_{M,i} = \frac{-k_{1d} \pm \sqrt{k_{1d}^2 - 4m_1 k_{1p}}}{2m_1} \tag{2.61}$$

where the plus sign is used for the first pole ($i = 1$) and the minus sign is used for the second pole ($i = 2$).

In order for the system to be stable, the poles must have a negative real part, which yields the condition

$$0 \geq -4m_1 k_{1p} \tag{2.62}$$

which is always verified, since m_1 and k_{1p} are positive constants.

To avoid transitional oscillations before settling, real poles are preferable, which gives the following additional condition

$$k_{1d}^2 \geq 4m_1 k_{1p}. \tag{2.63}$$

Figure 2.8 is a graphical representation of (2.63) where the region above the curve satisfies the inequality.

From (2.60), the pole for the mini is given by

$$p_{m,1} = \frac{-c_r}{m_r} \tag{2.64}$$

which is always real and negative since c_r and m_r are positive real constants.

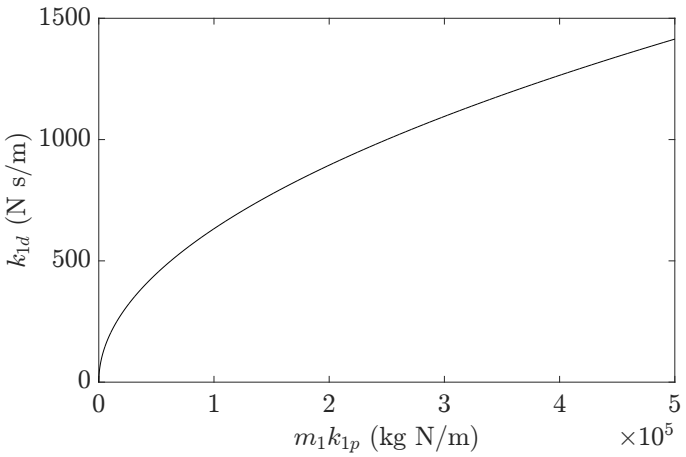

FIGURE 2.8 – Critical value of k_{1d}.

2.7.5 Zeros

From equation 2.58, the zero for the macro is given by

$$z_M = \frac{-k_{1p}}{k_{1d}} \tag{2.65}$$

Fig. 2.9 shows the response for (2.57) to a unit step input in x_3. k_{1d} is present in both the pole

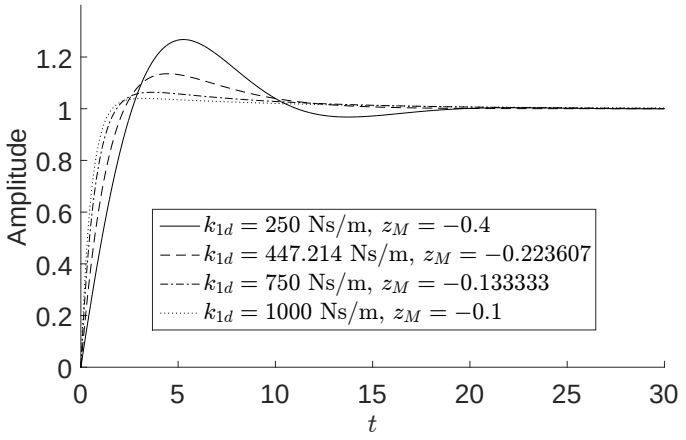

FIGURE 2.9 – Equation 2.57 : response to a unit step input in x_3, for different values of k_{1d}. $m_1 = 500$ kg and $k_{1p} = 100$ N/m.

and the zero for the macro control law. Increasing k_{1d} reduces the overshoot or oscillations and increases the time required to settle from its presence in the pole (denominator), but increases the time response from its presence in the zero. In theory, k_{1d} could be increased as much as possible. In practice, it will be limited by the noise of the velocity signal.

From (2.60), the mini has obviously no zeros.

2.8 Assessment of the performance of the macro/mini robot

2.8.1 Determination of the Required Range of Motion of the Mini Robot (L)

In a context of design, it is desired to determine the range of motion of the mini robot (L) that will allow a proper rendering of the virtual mass to the user while keeping the mini robot as compact as possible. In other words, it is important to determine the value L that allow all desired harmonic motion frequency without the macro lagging behind the mini sufficiently to hit its physical limits. To this end, the dynamic models and controllers derived above are used. Table 2.1 gives the specific values used for the different relevant parameters and Table 2.2 gives the different limitations of the system. The values of the parameters are selected based on typical industrial assembly line operations, where large components must be manipulated by human operators with the help of a macro-mini robotic system (see for instance [3]). In fact, the use of an active mini robot is justified by the large size and mass of the components to be manipulated, for which a passive mini robot such as the one presented in [3] cannot be used because the forces required from the human user would be too large.

TABLE 2.1 – Parameters used.

m_1	kg	500
m_2	kg	100
m_r	kg	10
c_r	Ns/m	5
k_{1p}	N/m	500
k_{1d}	Ns/m	5000

TABLE 2.2 – Limitations.

$f_{1,max}$	N	900
$f_{2,max}$	N	450
$f_{h,max}$	N	50
$\dot{x}_{1,max}$	m/s	1
$\ddot{x}_{1,max}$	m/s/s	1
$\dot{x}_{3,max}$	m/s	1
$\ddot{x}_{3,max}$	m/s/s	5

Figs. 2.10 and 2.11 illustrate the different limitations introduced in Section 2.6 for different values of the range of motion L, where R_h stands for the maximum amplitude of harmonic motion that can be produced at the end-effector without exceeding the capabilities of the human operator. Similarly, R_v, R_a, R_1 and R_2 represent respectively the maximum amplitudes corresponding to the velocity limitation of the macro robot, the acceleration limitation of the macro robot[1], the force limitation of the macro robot[1] and the force limitation of the mini robot. R_s corresponds to the maximum amplitude of harmonic motion that can be produced without exceeding an end-effector velocity of $1\,\mathrm{m\,s^{-1}}$ (safety standard).

The results of simulations performed at different frequencies are also included on the plots. The simulations were performed by prescribing a harmonic motion to x_3. For a given frequency, the

1. The curves for R_a and R_1 are very close to one another and difficult to distinguish on the graphs.

amplitude A_3 was increased gradually. Once steady-state was achieved, the highest amplitude A_3 reached, before the mini robot x_2 reaches at least one of its limits, is noted. It should be pointed out that the input harmonic motion used for the simulations is not necessarily feasible, *e.g*, at high frequency when it is above the R_h curve. Indeed, with the maximum sustainable human force chosen, the high-frequency simulation results could not be reached by the operator. Nevertheless, the macro-mini system should theoretically be able to produce them.

The curves for R_h and R_2 are identical for the parameters given in Tables 2.1 and 2.2. Indeed, the value for m_r chosen in Table 2.1 corresponds to its minimum possible value, as given in (2.45). For a given frequency, all amplitudes of motion of the end-effector that fall under all curves should be theoretically possible, given the mentioned limitations.

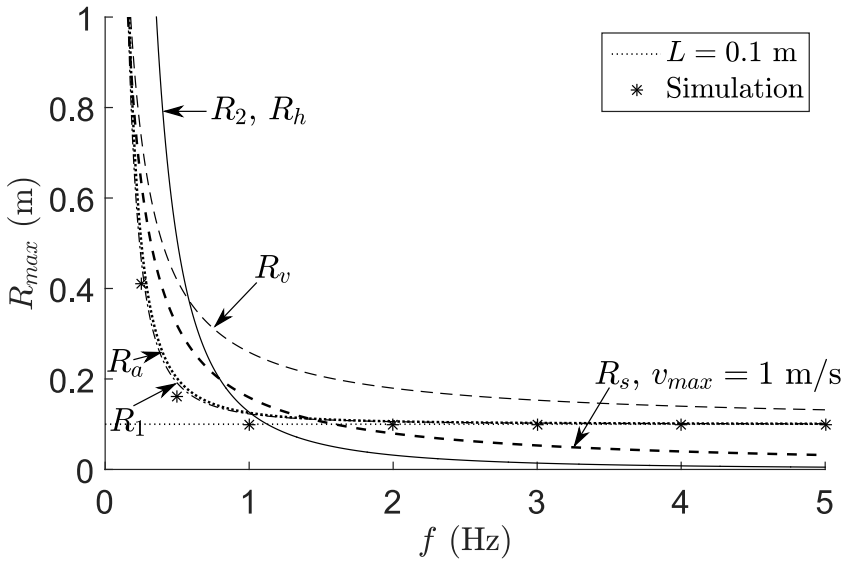

FIGURE 2.10 – Limitations for $L = 0.1$ m.

Figs. 2.10 and 2.11 show that the limiting curves are R_1, R_h (which coincides with R_2) and R_s, for the given parameters. Since R_s and R_h are imposed by safety and ergonomic standards, the goal is then to choose a value of L with the shortest frequency range in which the curve R_1 is the limiting factor.

It can be observed, in Figs. 2.10and 2.11, that increasing L shifts the curve R_1 towards higher values of R_{max}. The critical value of L, *i.e.*, L_c is the minimum value of L for which the curve R_1 is located above the curve R_s for all frequencies, meaning that the input motion becomes limited only by the human force and the safety standard and not by the system's limitations. It is equivalent to the value of L for which the curves R_1 and R_s touch in a single point. L_c is then obtained by equating (2.39) and (2.47) and solving for ω. The value of L that gives a

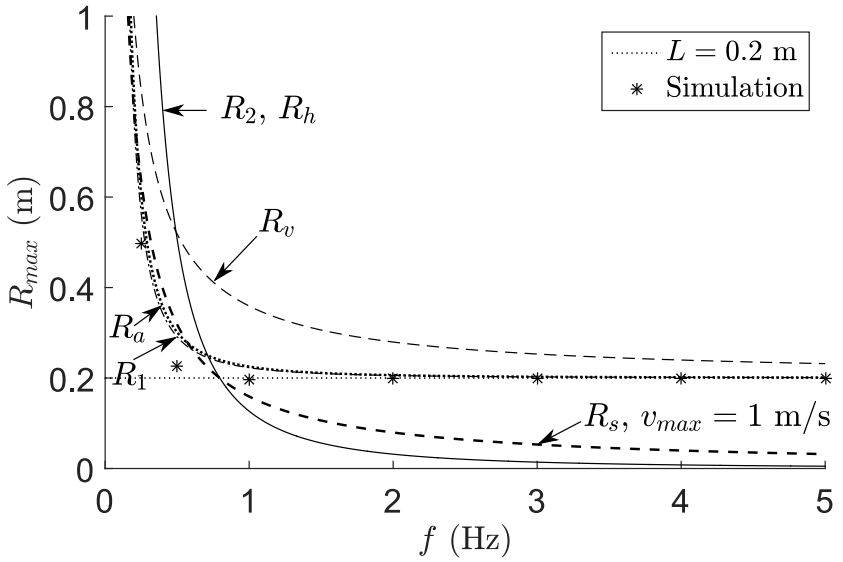

FIGURE 2.11 – Limitations for $L = 0.2$ m.

single root is given by

$$L_c = \frac{m_1 \dot{x}_{3,max}^2}{4(f_{1,max} - f_{2,max})}. \tag{2.66}$$

For the values of the parameters given in Tables 2.1 and 2.2, (2.66) yields $L_c = 0.2778$ m, shown in Fig. 2.12.

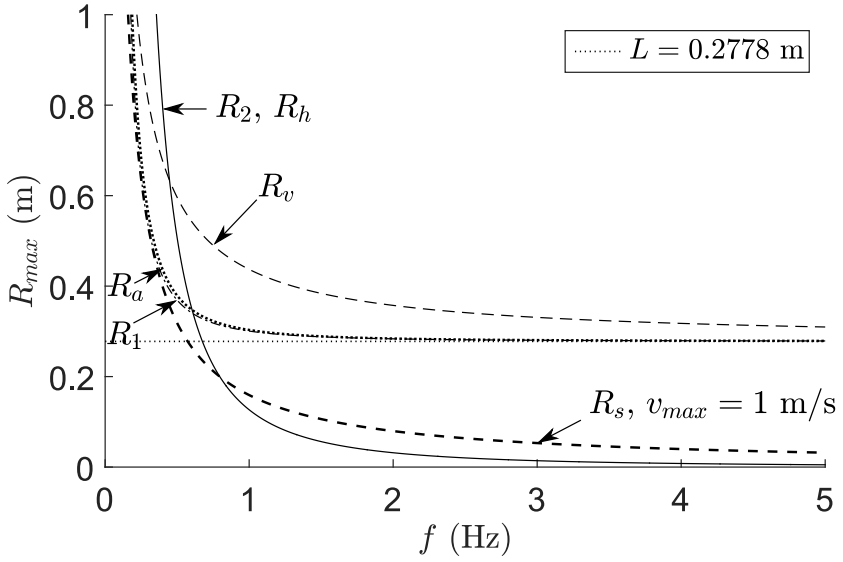

FIGURE 2.12 – Limitations for $L = 0.2778$ m.

As expected, Figs. 2.10, 2.11 and 2.12 show that increasing L increases the amplitude of the end-effector motion that the system can follow without hindering the motion for a given

frequency. Of the three results presented, Fig. 2.11 ($L = 0.2$ m) yields the smallest frequency range in which the macro is the limiting factor.

On the other hand, increasing L requires a larger and heavier mini robot, which in turn requires more powerful actuators. This increases the moving mass of the payload, so it adds mass to both the macro robot and the mini robot. Therefore, a compromise should be reached in the design of the mini robot and the analysis and discussion presented above can be used to determine this compromise.

2.8.2 Phase Shift Between the Macro and the Mini

Figs. 2.10 and 2.11 provide highly valuable insight on the design of the macro-mini robot. However, these results are based on the limitations presented in section 2.6, which have been derived from the assumption that the macro and the mini are perfectly in phase (*i.e.*, $\phi = 0$). Simulations show that this is generally not the case in practice, as illustrated in Fig. 2.13.

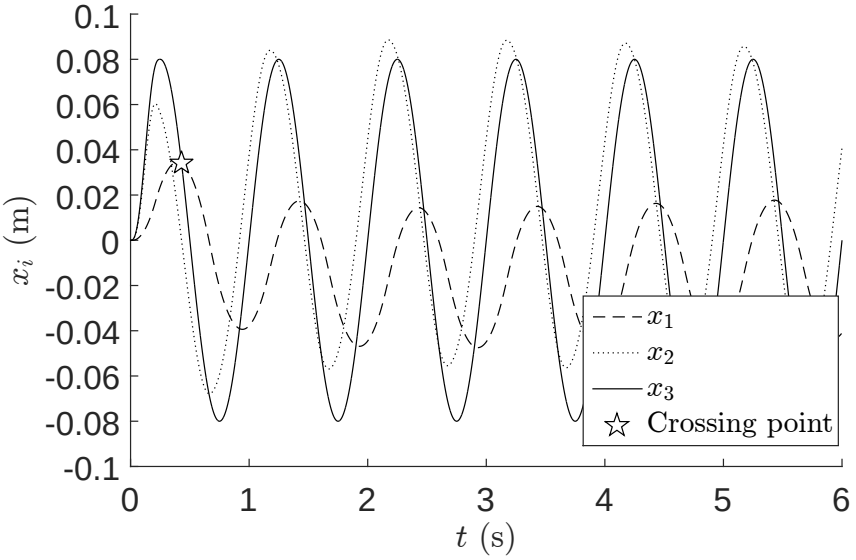

FIGURE 2.13 – Simulation of the macro-mini system for a harmonic input motion ($A_3 = 0.08$ m and $\omega_3 = 2\pi$ rad s^{-1}). The macro and mini robots are initially at rest.

The simulations were conducted as follows. From a *Simulink* model using the controller presented in Section 2.7, a harmonic motion of a given frequency is prescribed to x_3. The amplitude A_3 is chosen within the kinematic limitations described before. Both the macro robot x_1 and the payload x_3 are initially at rest.

Equation (2.22) gives an expression for the amplitude required by the mini for a given amplitude of input motion, amplitude of macro motion and the phase between the two. Equations (2.30) and (2.31) inform on the maximum achievable amplitude for a harmonic motion, given a maximum velocity and a maximum acceleration possible for the macro, respectively.

The same equations can be used for the payload, changing the subscript from 1 to 3. Then, the maximum amplitude reachable is the lowest of these two values. In other words, knowing the maximum velocity and maximum acceleration for the macro and the payload, the maximum reachable amplitudes for a given frequency can be computed with

$$A_{i,max} = \min\left(\frac{\dot{x}_{i,max}}{\omega}, \frac{\ddot{x}_{i,max}}{\omega^2}\right). \tag{2.67}$$

Knowing $A_{3,max}$ and assuming $A_{1,max}$, the only unknown that remains is ϕ in order to observe the behaviour of A_2 with respect to frequency. An expression for ϕ is then needed.

From the controller presented in Section 2.7, it can be assumed that the macro changes direction when the mini crosses its path, shown as a star on Fig. 2.13. Knowing that, a theoretical phase can be computed from the angle at which x_3 reaches $A_{1,max}$ after the initial peak at 90 °. It should be pointed out that this assumption is not exactly correct since (2.50) contains a velocity-dependent term as well as a position dependent term. Fig. 2.13 shows that the peaks of x_1 occur before x_3 crosses the x_1 curve, but choosing its peak value in $x_3(t)$ provides a good approximation for an upper bound of the phase. Mathematically, the phase is then given by

$$\phi \simeq \arcsin(A_{1,max}/A_{3,max}) - \frac{\pi}{2} \tag{2.68}$$

Clearly, this approximation for ϕ is only justifiable when $A_{1,max} < A_{3,max}$.

Another way to obtain the values for ϕ is through the simulations. By prescribing A_3 to the value given by (2.67) and the simulated response from the macro robot, the values of ϕ can be inferred once the steady-state is achieved for different frequencies. The results are shown in Fig. 2.14.

For each value of the maximum velocity, Fig. 2.14 shows three distinct frequency ranges in which the behaviour for ϕ is different, for both the approximation and the simulations. These frequency ranges are divided by the dotted vertical lines, the two with a circle at their base for $\dot{x}_{3,max} = 1$ m/s and the two with a diamond at their base for $\dot{x}_{3,max} = 0.5$ m/s.

The first range, on the left in Fig. 2.14 where the frequencies are low, is characterized by $A_{1,max} \geq A_{3,max}$. In practice, since the macro is programmed to follow the mini, A_1 is quite comparable to A_3, which yields a straight line, *i.e.*,

$$\frac{A_{1,max}}{A_{3,max}} \approx 1. \tag{2.69}$$

This first frequency range ends when the acceleration limit of the macro crosses the velocity limit of the mini. It happens when $A_{1,a} = \ddot{x}_{1,max}/\omega^2$ equals $A_{3,v} = \dot{x}_{3,max}/\omega$, from (2.67). The frequency at which this condition is met is given by

$$\omega_{c,13} = \frac{\ddot{x}_{1,max}}{\dot{x}_{3,max}}. \tag{2.70}$$

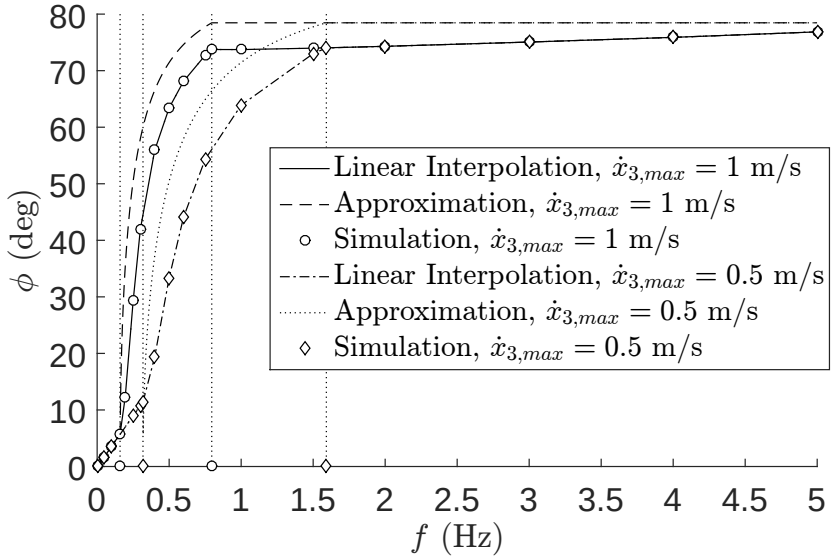

FIGURE 2.14 – Phase between the macro and the mini, obtained from simulations for $\dot{x}_{1,max} = 1$ m/s, $\ddot{x}_{1,max} = 1$ m/s/s, $\ddot{x}_{3,max} = 5$ m/s/s. The approximation is calculated from (2.68).

The second frequency range, in the middle, is characterized by $A_{1,max} < A_{3,max}$. In this range, $A_{3,max}$ is given by its velocity limit while $A_{1,max}$ is limited by its acceleration, *i.e.*, from (2.67), $A_{3,max} = \dot{x}_{3,max}/\omega$ and $A_{1,max} = \ddot{x}_{1,max}/\omega^2$. The ratio $A_{1,max}/A_{3,max}$ is then given by

$$\frac{A_{1,max}}{A_{3,max}} = \frac{\ddot{x}_{1,max}}{\omega \dot{x}_{3,max}}. \tag{2.71}$$

Similarly to the first range, this frequency range ends when the acceleration limit of the mini crosses its velocity limit. This condition is met when $A_{3,a} = \ddot{x}_{3,max}/\omega^2$ equals $A_{3,v} = \dot{x}_{3,max}/\omega$, from (2.67). The associated frequency is then given by

$$\omega_{c,33} = \frac{\ddot{x}_{3,max}}{\dot{x}_{3,max}}. \tag{2.72}$$

For the third frequency range, on the right in Fig. 2.14, $A_{1,max}$ is still smaller than $A_{3,max}$. The difference with the previous frequency range lies in the fact that the mini is limited by its acceleration. In others words, in this range, from (2.67), $A_{3,max} = \ddot{x}_{3,max}/\omega^2$ and $A_{1,max} = \ddot{x}_{1,max}/\omega^2$. Then, the ratio of amplitudes is given by

$$\frac{A_{1,max}}{A_{3,max}} = \frac{\ddot{x}_{1,max}}{\ddot{x}_{3,max}} \tag{2.73}$$

which is constant, yielding another straight line.

As mentioned before, an expression for ϕ would allow an analytical understanding of the behaviour for A_2 at all frequencies of interest. The maximum value reached by A_2 in the frequency range of interest represents the minimum value needed for L for the macro to follow the mini without reaching its limits.

The approximation for ϕ derived before is useful, but it is nevertheless an estimation. A linear interpolation is then applied to the data to obtain a more accurate estimation of ϕ as a function of frequency. Then, from Fig. 2.14 and from (2.22) and (2.67), the graph of Fig. 2.15 can be constructed, illustrating the maximum amplitude required by the mini robot. In other words, Fig. 2.15 shows the value needed for L, for a given frequency, so that the macro robot can follow the mini robot without the latter reaching either of its physical limits, based on the kinematic limitations prescribed in Table 2.2.

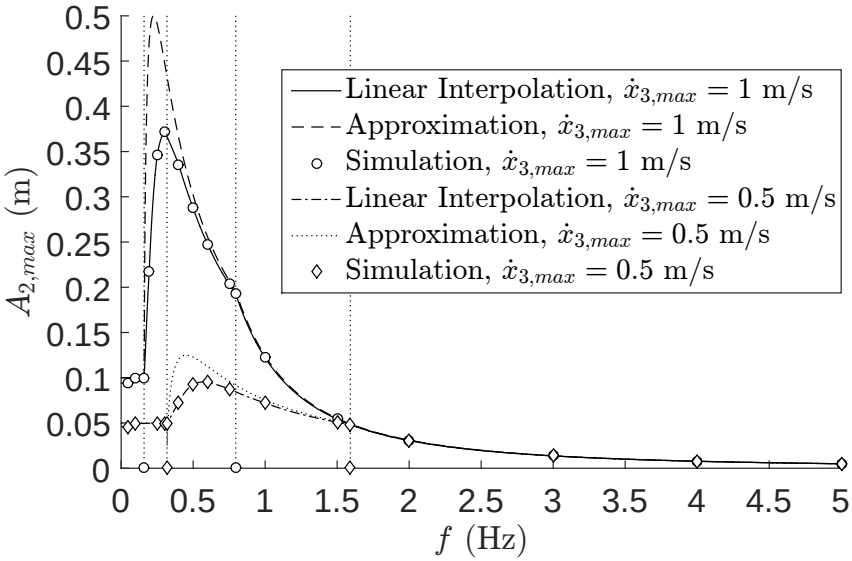

FIGURE 2.15 – Maximum amplitude needed from the mini for $\dot{x}_{1,max} = 1$ m/s, $\ddot{x}_{1,max} = 1$ m/s/s, $\ddot{x}_{3,max} = 5$ m/s/s.

Fig. 2.15 shows that, for the kinematic limitations presented in Table 2.2, the range of motion of the mini (L) should be approximately 0.38 m. Such a range would theoretically allow the macro robot to follow the mini robot, without hindering its motion.

In practice, however, a mini robot with a range of almost ± 0.4 m would be quite large and would add significant weight to both the mini robot and the macro robot. Also, other limitations related to the velocity of the payload must be considered, as explained in the next subsection.

2.8.3 Velocity Limitation of the Payload

Since a payload of 100 kg is assumed, the maximum velocity limit should reasonably be lower than $1\,\mathrm{m\,s^{-1}}$, for safety purposes. Indeed, the safety standard of $1\,\mathrm{m\,s^{-1}}$ is used for collaborative robots with payloads of the order of 10 kg, which represents a kinetic energy of 5 J. If a similar kinetic energy is assumed for a payload of 100 kg, the payload velocity should be limited to approximately $0.32\,\mathrm{m\,s^{-1}}$. Figs. 2.14 and 2.15 show the results for a simulation

with a maximum payload velocity of $1\,\mathrm{m\,s^{-1}}$ as well as one with a maximum velocity of $0.5\,\mathrm{m\,s^{-1}}$. Adding this limitation to Fig. 2.11, it can be shown that this new limitation would be dominant, up to approximately 1.6 Hz, as shown in Fig. 2.16. Fig. 2.15 shows that the

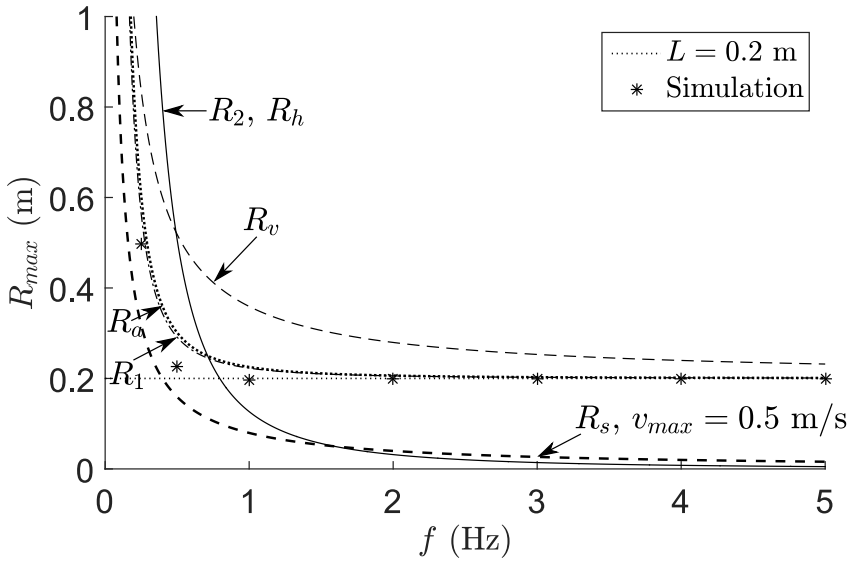

FIGURE 2.16 – Limitations for $L = 0.2$ m, with $v_{max} = 0.5\ \mathrm{m\,s^{-1}}$.

maximum value reached by the curve for the linear interpolation of the maximum velocity of $0.5\,\mathrm{m\,s^{-1}}$ is slightly under 0.1 m. This means that reducing the maximum velocity by a factor of 2 reduces the range of motion needed for the mini robot by a factor of almost 4. As expected, reducing the maximum velocity reduces the maximum value needed for L. This means that knowing the maximum allowable velocity for a payload of the order of 100 kg is important.

2.8.4 Discussion

From the values presented in Table 2.2 and the different figures shown, the kinematic limitations (*i.e.*, those from the chosen acceleration and velocity) are the most limiting ones in the range of frequency where a large value of L is required. Future experimental validation will help to determine if the chosen values are reasonable.

The ideal case of $\phi = 0$ gave interesting insight toward determining the range of motion L necessary for the mini robot. However, this case is unrealistic. Simulations were then conducted using the simple controller presented in Section 2.7. These simulations allowed to take into account the phase shift between the macro robot and the mini robot during simple harmonic motion. By considering the phase shift and the mathematical models derived in Section 2.5, the amplitude A_2 was plotted as a function of the frequency in Fig. 2.15, for the values chosen in Tables 2.1 and 2.2. It can be observed that the maximum value reached by A_2 is approximately 0.4 m for a maximum payload velocity of $1\,\mathrm{m\,s^{-1}}$ and approximately 0.1 m for a

maximum payload velocity of $0.5\,\mathrm{m\,s^{-1}}$. Therefore, by dividing the maximum payload velocity by 2, the range of motion needed for the mini robot is divided by a factor of approximately 4.

2.9 Conclusion

This paper studied the impact of the range of motion of an active 1-dof mini robot on the possible motion that a human user can impart to the payload. Mathematical models for the active macro/active mini system were presented. Different limitations were considered, such as safety standard, maximum human force, maximum kinematic and dynamic capabilities, in order to determine the maximum feasible motion of both the active macro robot and the active mini robot. An ideal case (perfect synchronization) was first investigated. Then, the phase shift between the macro robot and the mini robot was considered in the equation. Simulations were conducted using a simple controller to determine the effect of the phase shift on the maximum amplitude needed for the mini.

For the values used in this study, a mini robot with a range L of almost $0.4\,\mathrm{m}$ is required to allow all possible payload motion up to a velocity of $1\,\mathrm{m\,s^{-1}}$, corresponding to the safety standard for collaborative robots. Such a mini robot would be quite large. Simulations showed that reducing the maximum velocity by one half reduces the value of L needed to about a quarter, which is a more reasonable size for a mini robot. The motivation behind the reduction in maximum velocity stems from the large payload assumed in this study. Safety standards for collaborative robots are based on payloads of the order of $10\,\mathrm{kg}$ rather than $100\,\mathrm{kg}$. A payload of $100\,\mathrm{kg}$ moving at $1\,\mathrm{m\,s^{-1}}$ would indeed be very impressive and probably be perceived as unsafe by a human user.

The mathematical models and the simulations provided highly valuable insight for the selection of the required range of motion L required based on the frequency range of interest. In the future, experimentations will help to confirm (or to question) the hypotheses and assumptions used in this paper.

Chapitre 3

Haptic Interface for Handshake Emulation

3.1 Résumé

Cet article introduit un prototype d'interface haptique conçu pour produire une poignée de main réaliste entre un humain et un robot. Inspiré par l'anatomie de la main humaine, une nouvelle main robotique conçue pour offrir une compression de la paume et une fermeture des doigts réaliste est présentée. Puisque le système est rétrocommandable, une boucle de contrôle en position avec rétroaction est implémentée pour produire un comportement similaire à celui d'une main humaine. Les déplacements du bras sont produits par un manipulateur sériel collaboratif. Ce manipulateur utilise un contrôle en impédance autour d'une trajectoire sinusoïdale pour simuler une intention ou une personnalité. Le nouveau prototype améliore celui proposé par les auteurs de travaux précédents, offrant une utilisation plus facile, plus efficace, plus robuste et plus confortable tout en offrant le mouvement du bras actif. L'expérimentation est réalisée pour déterminer l'impact de différents paramètres de la trajectoire, *i.e.*, la fréquence, l'amplitude et les coefficients d'amortissement et de raideur, sur le réalisme perçu de la poignée de main. Il est démontré que l'amplitude n'a pas d'impact dans l'intervalle étudié (10 à 30 mm) et qu'une fréquence d'environ 2 Hz est préférable. Les intervalles de valeurs pour les coefficients d'amortissement et de raideur offrant les meilleurs résultats sont également identifiés. L'expérimentation permet également d'identifier des améliorations potentielles pour le prototype dans le futur.

3.2 Abstract

This paper introduces a prototype of a haptic interface designed to produce a realistic human-robot handshake. Inspired by the human hand anatomy, a new robotic hand designed to achieve a realistic palm compliance and finger grasping is presented. As the system is back-

drivable, a position-controlled feedback loop is implemented to render a human-like hand behaviour. The overall arm motion is achieved through a collaborative serial manipulator. This manipulator uses an impedance control around a sinusoidal trajectory to simulate its intention or personality. Improved from the design proposed by the authors in previous work, the new prototype is easier to use, more efficient, more robust and more comfortable with an active arm behaviour. Experiments are then performed to determine the impact of different trajectory parameters, such as frequency, amplitude, and damping and stiffness coefficients, on the perceived realism of the handshake. It is shown that the amplitude has no impact in the range studied (10 to 30 mm), while a frequency of approximately 2 Hz is preferred. Ranges of values of the damping and stiffness coefficients yielding the best results are also determined. The experiments also allow the identification of potential improvements to be implemented on the prototype in the future.

3.3 Introduction

As one of the most popular greeting gestures, the handshake plays an important role in western cultures [31]. The action of handshaking can be described as a ritual requiring a coordinated effort between both participants [32]. Furthermore, a particular handshake is characterized or influenced, in part, by one's personality, mood, gender, etc. [33] Given how much information or insight can be transmitted, the simple act of handshaking is perfectly suited to explore and research haptic devices and collaborative robotic controls. This paper focuses on the design of a robotic hand mounted on a collaborative serial manipulator to achieve a realistic and natural human-robot handshake.

The simple motion of a handshake between two people in different contexts has been studied in the past [34; 35]. It has been described as an oscillatory motion lasting for a few cycles, at a frequency of about 2 to 2.5 Hertz.

The handshake experience between a human and a robot has been previously researched. Some papers focus mostly on the grasping aspect, while others report on the actual arm motion.

For instance, references [36] and [37] consider the hand behaviour of a handshake, more precisely the fingers' grasp in relation to the palm compression. The former reference uses an admittance controller which yields good results, but slow response times. The latter reference is based on an impedance controller to obtain human-like agility, but provides insufficient forces due to the mechanical design.

As mentioned above, a handshake can be described as a coordinated effort between two participants. This means that both participants must strive to reach a synchronization in order to produce a natural motion. In simpler terms, they must adapt to one another. Different means have been studied to solve this problem. Used for rhythmic motion, neural oscillators are em-

ployed to synchronize and control the handshaking motion between a human and a robot from the joint torques [38]. However, neural oscillators require many parameters to be determined which are related to each other. In [39] and [40], the dynamics of the system are designed from a polynomial approximation to create a vector field converging on an attractor trajectory. The forces applied by the human are used as an input signal to update the dynamics online and reach synchronization of a given strength. References [41] and [42] studied the approaching and leading motions of a handshake, i.e., the motion taking place before contact is made between the participants and the initial direction of oscillations, respectively. The former is a function of the measured human arm motion and the latter depends on the height at which contact is made. The actual shaking motion is produced with the robot following the human, with given impedance parameters, to reach synchronization. A Hidden Markov Model can also be used to infer the human intention from the online estimated impedance parameters of the human [43]. The human intention inferred is used to adapt the reference trajectory of an admittance position controller to reach synchronization.

In [44], [45] and [46], an interesting method to evaluate the realism of a human-robot handshake is presented. In summary, the method consists in transmitting a handshake between two linked haptic devices such that two people can shake hands remotely. The subjects are asked to assess the quality of a handshake, while being unaware of whether there is a human on the other side or whether the handshake is artificially generated. Such bilateral haptic devices have also been studied in [47; 48; 49].

The references mentioned above yield good results — with a varying level of success — for the grasping action or the motion synchronization. However, both of these aspects are not combined and most of the synchronization methods simply end up with the robot following the human. The “personality" or the intent of the robot is not really taken into consideration.

The current project aims to combine the hand and the arm behaviours as well as to simulate a personality and mood to achieve a complete and natural handshake experience. To this end, the prototype previously proposed by the authors in [37] was improved to be easier to use, more efficient, more robust and more comfortable with an active arm behaviour. A user study was also conducted to determine the arm trajectory parameters considered the most natural. This study will then be used in future work to design a controller to hopefully reach a harmonized motion between the human and the robot.

This paper describes a first step toward a unified and natural handshake interface and is structured as follows. In Section 3.4, the objectives of the research are stated. The mechanical design of the proposed prototype is then presented in Section 3.5. The structure of the controller and the control approach are exposed in Section 3.6. In Section 3.7, the experiments conducted with the handshaking haptic device are described and the results obtained are analyzed. Finally, conclusions and suggestions for future work are given in Section 3.9.

3.4 Objectives

The concrete long-term objective of this project is simple : to produce a natural and realistic handshake between a human and a robot. In order to fulfill such an ambition, one must start with a smaller, intermediate goal in mind and build towards this global objective. This paper then focuses on a first step towards a natural and realistic human-robot handshake : quantify and qualify what makes a handshake natural. To address this problem, one can subdivide it into smaller tasks.

First, a prototype (i.e., a robotic hand) must be designed to emulate the grasping behaviour. This prototype should be mounted on a robot arm to emulate the arm motion.

With a functional prototype, experimentation can be conducted and data, gathered. These data can then be used to infer different characteristic parameters or aspects of a handshake deemed natural and realistic. The experimentation also allows the identification of modifications or improvements to achieve the final goal.

As mentioned above, the authors have studied the human-robot handshake in previous work [36][37], which has provided significant insight. In this paper, a new prototype is presented that addresses the shortcomings of previous prototypes and a new control approach is used. Also, in previous work the robot on which the handshaking device is mounted was playing a passive role while it is playing an active role here, which makes it possible to adjust the “personality" of the robot.

3.5 Mechanical Design

The aforementioned steps required to work toward a realistic human-robot handshake begin with the design of a mechanical hand.

The prototype conceived for this project is composed of a custom robotic hand mounted on a robot arm. The robot arm used is a *Kuka LWR 4+*, a collaborative serial manipulator with seven degrees of freedom.

This section describes the mechanical changes and improvements made to the previous prototype presented in [37]. For purposes of presentation, the robotic hand mechanism can be divided into three parts : the overall design, the fingers and the palm, described below.

3.5.1 Overall Design

The previous prototype was actuated by two Pittman electric motors, one for the palm (9236S009) and the other for the fingers (GM9236C534-R2). The latter used a 5.9 :1 gear reduction to increase the grasping force achieved. In order to yield acceptable forces at the fingers and the palm, the motors were used above their load limit and they tended to overheat.

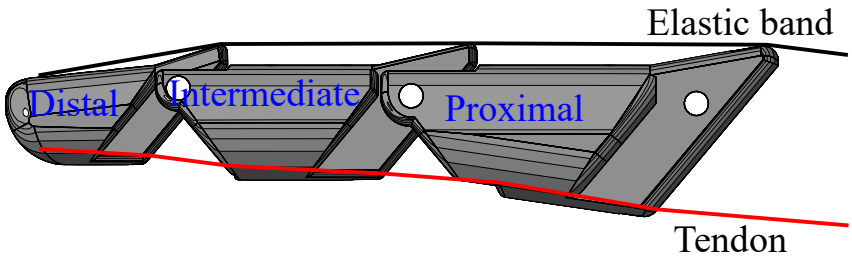

FIGURE 3.1 – Mechanical design of the fingers.

For this reason, the actuators were replaced. In the prototype presented here, the fingers' actuator is a Maxon EC 90 Flat brushless electric motor with a 6400 counts per turn encoder. The palm's actuator is a Maxon EC 45 Flat brushless electric motor with a 2048 counts per turn encoder. Both of these motors are mounted with a direct drive transmission and used within their respective limits. Other than the motors' encoders, there are no sensors.

In the previous design, both motors were located on the same side of the hand and the slider mechanism prevented the shafts from being doubly supported. In the current prototype, the motors are mounted on each side of the hand in order to keep the centre of mass of the hand close to its geometric centre. The relocation also allows both motor shafts to be doubly supported.

In the previous prototype, most components were made of 3D-printed ABS plastic. Due to the material and design, many parts were prone to warping and breaking. Hence, the mechanical parts have been redesigned for comfort, durability, robustness and ease of use/assembly. Most of the finger and palm parts are relatively complex and are not subjected to excessive forces, so ABS plastic was used for these parts in the new design. However, the structural components of the new prototype are made of aluminum. This includes the frame of the hand, on which the motors are mounted and the palm links, which are subjected to most of the loading from the human user. The shapes of these parts are simple, which facilitates machining.

3.5.2 Finger Design

During the handshake, the human user's hand is grasped by the prototype's fingers. Similarly to the previous prototype, the robotic hand has a passive thumb and three actuated fingers. The latter are the index, the middle finger, and the ring and little fingers merged into one. For directness, the third finger is simply referred to as the ring finger in what follows. The choice of three fingers, instead of four, is based on a space constraint.

Just like in the human hand, each finger has three phalanges, namely the distal, intermediate and proximal phalanges, as shown in Fig. 3.1. Its actuation is achieved from a cable, running from the fingertip to the base, acting as a tendon. When the cable is pulled, the finger folds

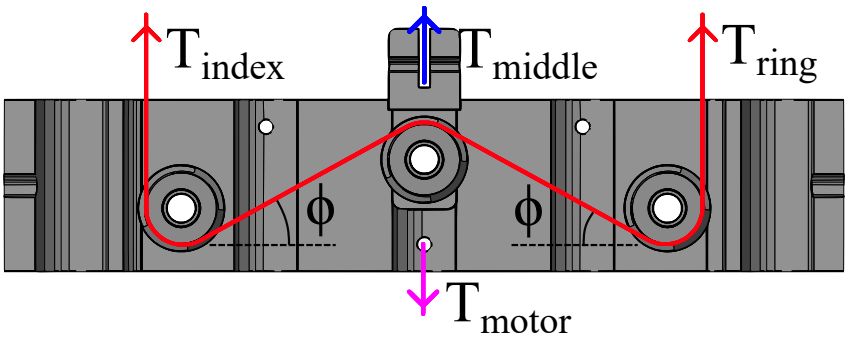

FIGURE 3.2 – Pulley system to distribute the motor force.

up to a closed position. An elastic band attached to the back opens the finger when the cable is released.

The previous prototype used a 1-DOF, semi-passive semi-actuated, thumb. In order to actuate the thumb, a lever at its pivot and a cable to the slider were used in tandem. The thumb's cable was attached to the slider through a spring and not to the pulley system. The spring was used to ensure that the thumb's closure did not interfere with the fingers'. In such an arrangement, the spring has to be soft enough so that it does not stop the fingers from closing further when the thumb makes contact. The lever was uncomfortable, poking the human's hand, and the 1-DOF thumb could not adapt well to different hand shapes and sizes. The thumb actuation was not ideal.

In the prototype proposed here, the thumb was redesigned to add a second DOF and improve the adaptability and comfort. The thumb is now passively driven, meaning that it is not actuated by a motor, but by the compression of the palm. Its cable wraps around a pulley and is attached to the opposite finger, i.e., the ring finger. Therefore, if the palm is not strongly compressed, the thumb does not press much on the human hand.

All three fingers are controlled by the same motor, i.e., the mechanism is underactuated. As with the earlier design [37], a system of pulleys, illustrated in Fig. 3.2, is used to distribute the fingers' motion. This system is required so that the fingers can adapt independently to the shape and size of the objects (here the human hand) being grasped. Such underactuated transmissions are common in prosthetic and robotic hands and can be implemented using gears, levers and other means.

In the previous prototype, the slider guides used to slide out of the hand's frame during operation and dowel pins were used as pulleys inside the slider. In the prototype proposed here, the slider has then been redesigned to accommodate pulleys in order to minimize friction and all components are now fully enclosed within the hand's frame.

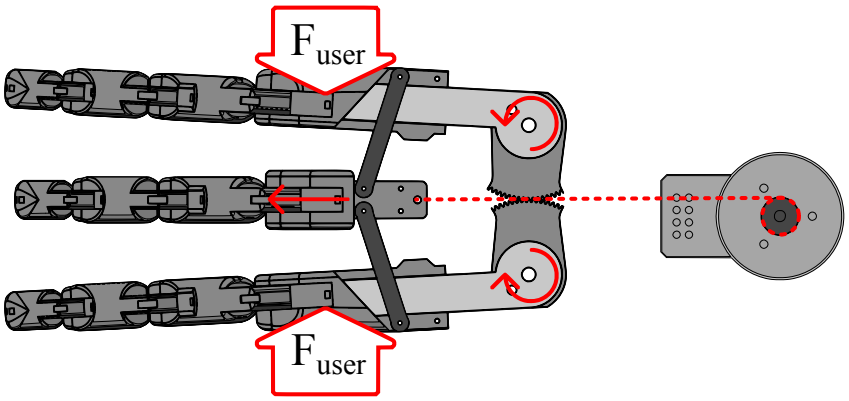

FIGURE 3.3 – Mechanical design of the palm.

3.5.3 Palm Design

The palm plays a significant role in achieving a realistic handshake. Obviously, the palm is the part of the prototype that the user grasps. For this reason, it is important to get a realistic palm behaviour in compression.

Secondly, the prototype has no force or torque sensor. The grasping intent of the human user is detected and inferred from the palm position, i.e., its level of compression. In other words, the motion of the palm acts as an input for the control.

The human palm is composed of metacarpal bones, linking the proximal phalanges to the carpal bones [50]. These metacarpal bones can pivot on the carpal bones to spread or compress the palm, resembling the opening or closing motion of a hand fan.

The current prototype improves on the lever design proposed in [37]. The palm is composed of two symmetric levers to which the index and ring fingers are attached, as shown in Fig. 3.3. Instead of the three bars connecting the levers to the middle finger used in the previous prototype, two bars and a cylindrical guide are used in the new design. In the previous prototype, the middle finger was aligned relative to the index. It now remains on the symmetry axis between the two levers, yielding a linear motion.

In the previous prototype, the disk and bar mechanism used to transmit the middle finger motion to the motor was not efficient and was prone to reaching a singularity and to breaking when the palm was strongly compressed. This problem is solved in the current prototype by replacing the disk and bar mechanism by a simple cable and pulley system. Also, combined with the linear motion achieved above, the pulling force on the middle finger is independent from the motor angular position. Finally, it should be mentioned that, similarly to the previous prototype, the palm mechanism of the new prototype is backdrivable.

The conversion from the motor angle to the lever angle is obtained from a geometric analysis,

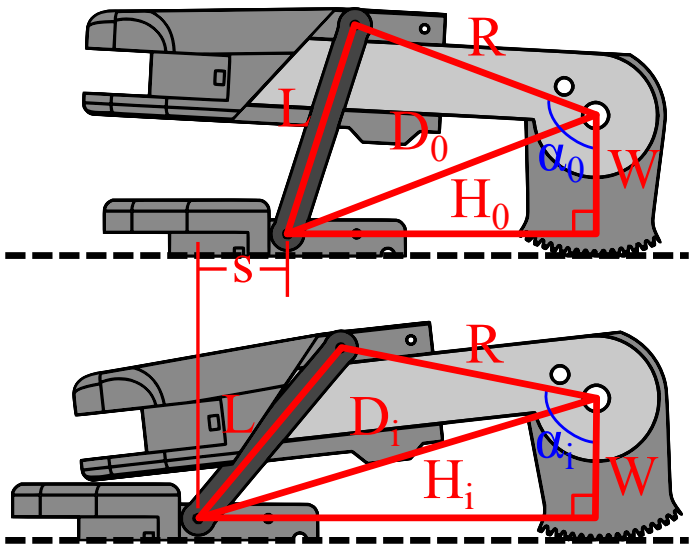

FIGURE 3.4 – Geometry of the palm transmission.

as illustrated in Fig. 3.4. The values L, R, W, H_0, and α_0 are known from the CAD model of the hand, where the subscript 0 denotes the initial position. Index i is used to represent an arbitrary configuration. The value of α_i can be found from (3.1), (3.2) and (3.3)

$$H_i = H_0 + s = H_0 + r_{motor}\theta_{motor} \tag{3.1}$$

$$D_i^2 = H_i^2 + W^2 \tag{3.2}$$

$$\alpha_i = \arctan\left(\frac{H_i}{W}\right) + \arccos\left(\frac{R^2 + D_i^2 - L^2}{2RD_i}\right) \tag{3.3}$$

where r_{motor} and θ_{motor} represent the radius and the angle of the pulley mounted on the motor's shaft, respectively.

3.6 Control

The control of the prototype can be divided into two components or controllers : the hand actuation and the arm motion, as described below.

3.6.1 Hand Actuation

The first controller is used to operate the robotic hand and is similar to the previous one [37]. Its role consists in sensing the handshake (the beginning, the end, the grasping action of the user) and, in return, gripping the user's hand with a given force.

As previously mentioned, there are no force, torque or tactile sensors on the robotic hand. The palm mechanism acts as an input device for the prototype.

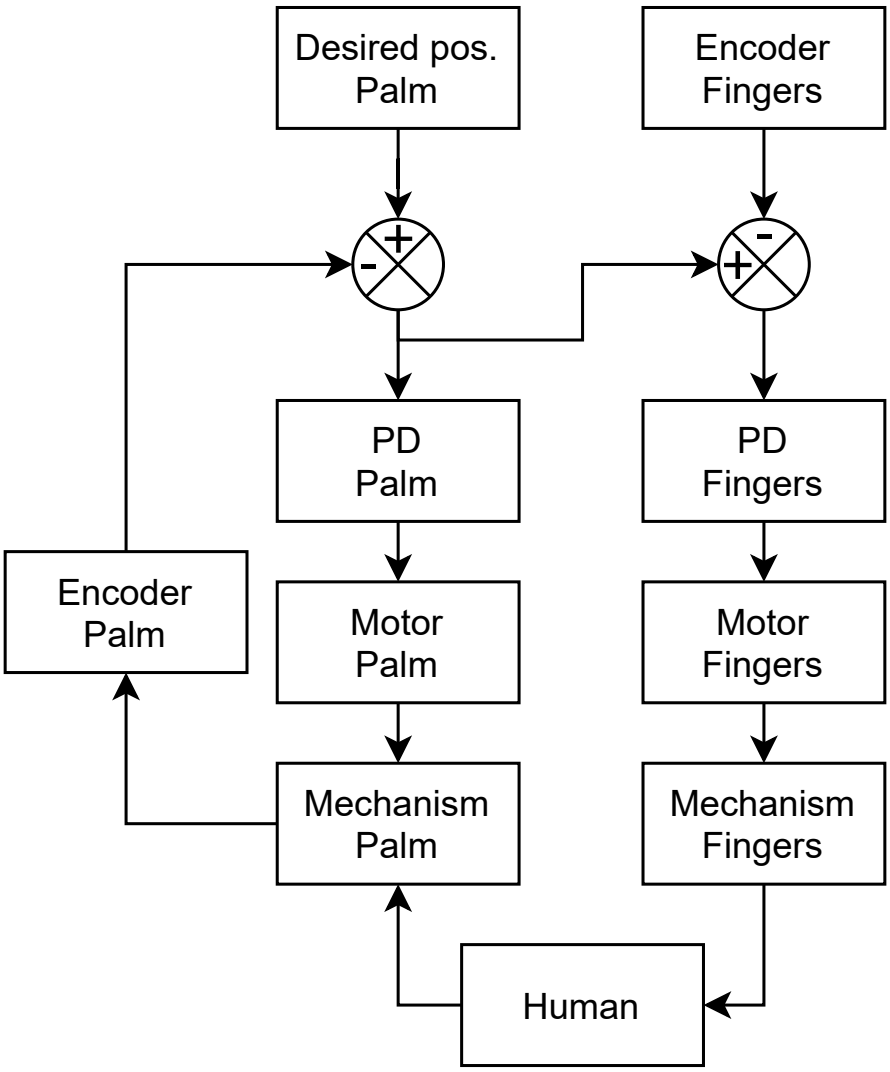

FIGURE 3.5 – Diagram of the system and control loop for the robotic hand.

A schematic representation of the system and control loop between the palm and fingers is illustrated in Fig. 3.5. Both the palm and the fingers use a position PD controller. A PD controller is simple to implement and yields good results for the application. The integral gain is not used to avoid the wind-up effect when the handshake is taking place. The desired position for the palm represents its initial open position.

The desired position for the fingers is proportional to the current position of the palm. Thus, the robotic hand grasps the user with a force proportional to the user's. The harder the user compresses the palm, the stronger the fingers close on his hand, up to a point defined by motor and safety limitations.

In other words, one can read Fig. 3.5 by starting at the human. The human grasp the robotic hand and compresses the palm. Therefore, the compression of the palm is detected by its enco-

der, inducing a difference between the palm current and desired positions. The PD controller then commands to the motor to try and bring this difference to zero.

The controller works similarly for the fingers. When the PD controller commands the finger motor, the motor pulls on the finger mechanism so the fingers grasp the human's hand.

The previous controller did not take into account the impact of the variable efficiency and variable transmission ratio of the palm mechanism on the force produced by the palm links. The desired compliance was achieved experimentally by choosing appropriate rubber pads.

The current hand controller translates the motor torque directly into the palm spreading torque. This feature, the choice of different motors and a constant palm transmission efficiency, allow the control of the palm compliance behaviour directly from the controller, without the need to mechanically alter the prototype.

3.6.2 Arm Motion

The second controller, which was not previously available in [37], provides the arm motion to the robotic hand. It manages the trajectory, or motion in space and time, of the handshake.

As important as the grasping hand is to achieve a natural handshake experience, the overall arm motion is most likely what makes or breaks the illusion. It is then imperative to be able to come up with a motion behaviour as close as possible to that of a real human. As mentioned earlier, the robotic hand is mounted on a collaborative serial manipulator, so it already resembles the human arm structure, as shown in Fig. 3.6.

For this reason, it is essential to observe the human-human handshake in order to define its motion. Reference [33] shows a correlation between one's personality traits and gender and some characteristics of one's handshake, such as strength, grip, vigour, dryness, eye contact, and others. This means that part of one's disposition or mood can be transmitted or one's temperament can be inferred from a simple handshake. To achieve a natural handshake, it is then important to simulate a given personality with consistent parameters.

The determination of the most relevant parameters in a handshake has been addressed in the literature ([34], [41], [38]). Based on observations, it is generally accepted in the literature that handshakes consist, for the most part, of simple oscillations, mostly in a vertical plane, lasting a few cycles. Given this information, one can easily estimate a handshake as a vertical motion, oscillating between a maximum height and a minimum height, which can be approximated by a periodic (e.g., sine) trajectory in time and height, defined using parameters such as frequency and amplitude.

In a standard handshake, two distinct roles can be identified, a leader and a follower [32]. In order to be able to play with these two roles, a simple impedance controller is implemented

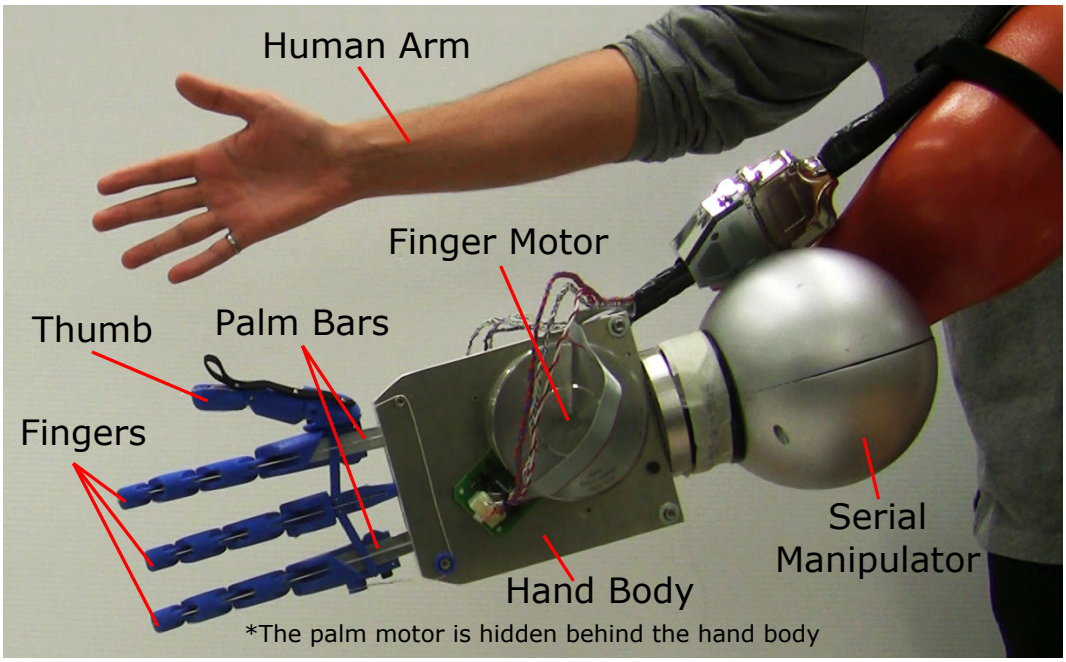

FIGURE 3.6 – Prototype and human arm side by side.

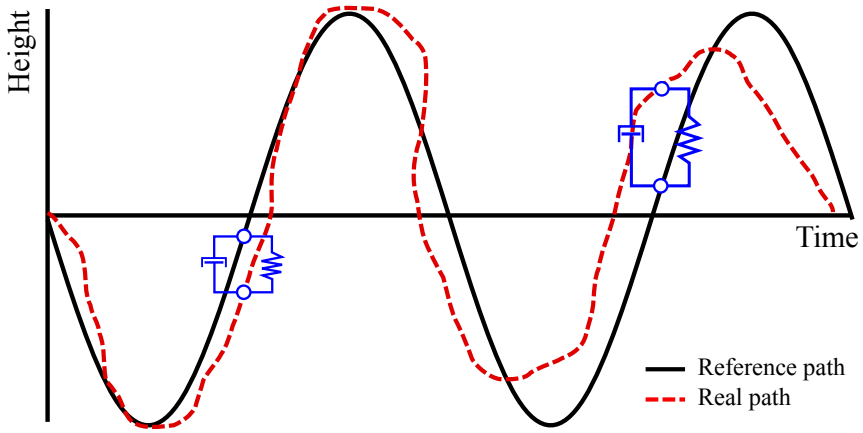

FIGURE 3.7 – Schematic representation of the arm control trajectory.

around the sinusoidal trajectory, yielding a force output for a given motion input. The impedance controller adds two parameters, stiffness and damping. A leader would have a high stiffness coefficient, resulting in higher forces confining the motion to the path, where a follower would have a low stiffness coefficient.

The control strategy is illustrated in Fig. 3.7. The real path represents the actual path travelled during the handshake and the reference path is the intent of the robot, or the path travelled without interference from the user.

As shown in Fig. 3.7, the reference path begins its motion in a downward direction. This direction is assumed natural from observation.

The initial simple control scheme is used to gather first-hand information on what is considered a natural handshake motion. Such information is useful to guide the future development of the project.

3.7 Experimental Results

As mentioned in Section 3.3, the subject of the handshake with a robot has been studied in the literature. Three main aspects are generally addressed, namely the hand grasping, the arm motion and the controller design. However, reported works typically address one or two of these issues only — not all three together — and very few of the references study the impact of the parameters on the realism of the handshake. Hence, experiments were conducted to observe the impact of different parameters on the perceived realism of different handshake motions. To introduce these experiments, the methodology is first presented, followed by the results and some pertinent observations.

3.7.1 Methodology

15 subjects (14 male and 1 female) were brought in to conduct the experimentation. Their age ranged between 20 and 50 years old. 10 of the subjects have a robotics background.

Each subject is brought in individually and briefly introduced to the project. A questionnaire, and sufficient time to read it, is given. The questionnaire asks for the subject's name and age, the date, followed by boxes to rate the different sets of handshake parameters. It also includes a list of questions.

The practical tests are then conducted at the subject's own pace, i.e., the subject can take as much time or as many trials as needed. Once all the tests are completed, the subject can answer the questions freely.

The controller used in this project includes four main parameters to define the handshake : the frequency, the amplitude, the damping coefficient and the stiffness coefficient. The frequency is chosen as the base parameter. The other three parameters are tested for different values of frequency.

The practical tests are conducted in the following manner. First, on a scale from 1 to 5 (5 being very natural and 1, not at all), the subject is asked to assess the realism of each set of handshake parameters that are tried.

For different values of frequency, various amplitudes are tried. Using the selected most natural amplitude, different damping coefficients are tried against the values of frequency. Finally, using the most natural amplitude and damping coefficient, different stiffness coefficients are tried for the same frequencies. The initial damping and stiffness coefficients are chosen based

Parameter	(X,Y)	F(X,Y)	p	Significant
Amplitude	(4,280)	1.1565	0.3303	No
Frequency	(3,280)	3.4124	0.0193	Yes
Interaction	(12,280)	0.5278	0.8961	No
Damping	(4,350)	4.2636	0.0022	Yes
Frequency	(4,350)	7.0031	1.9657e-05	Yes
Interaction	(16,350)	1.4836	0.1029	No
Stiffness	(4,350)	20.7545	2.3006e-15	Yes
Frequency	(4,350)	5.6491	2.0422e-04	Yes
Interaction	(16,350)	0.5575	0.9141	No

TABLE 3.1 – Two-way analysis of variance results.

on personal experience with the prototype.

The frequencies tested are 0, 1.5, 2, 2.5, and 3 Hertz. The amplitudes tested are 10, 15, 20, 25, and 30 millimetres. The damping coefficients tested are 20%, 40%, 60%, 80%, and 100%. The stiffness coefficients tested are 5%, 25%, 38%, 50%, and 100%. On the serial manipulator used, the stiffness and damping coefficients are vectors. Each component, associated with one of the seven joints, ranges from 0 to 2000 for the stiffness and from 0 to 1 for the damping. The stiffness and damping percentages used are ratios with respect to the maximum value applied to each component. The specific units are not known and are probably different for each joint, considering that all joints have the same range.

Obviously, the amplitudes are not tried with the zero frequency as it represents a fixed point and not oscillations.

In the end, each subject tested 70 different sets of parameters.

3.7.2 Results

Fig. 3.8 shows the average appreciation, or the level of realism selected by the subjects, for the three pairs of parameters studied, i.e., amplitude and frequency, damping and frequency and stiffness and frequency. As mentioned above, a higher score means a more natural handshake. The dashed lines are used to help visualize and differentiate the parameters studied.

A two-way analysis of variance was conducted to compare the main effect of each pair of parameters and their interaction effect on the perceived realism of the handshake. The results of the analysis of variance are summarized in Table 3.1. A significance level of 0.05 is used, i.e., an effect is deemed significant if its p-value is under this threshold. A test of main effects was then realized, shown in Table 3.2.

Regarding the amplitude and frequency parameters, all effects were not statistically significant except for the frequency. There is no significant difference between the amplitudes studied.

Parameter	Value Tested	Average Appreciation	Standard Deviation	Different from
Amplitude	10 mm	2.3958	0.9052	
	15 mm	2.6483	0.9334	
	20 mm	2.6550	0.9741	
	25 mm	2.5250	1.0465	
	30 mm	2.3517	1.1341	
Frequency	1.5 Hz	2.5800	0.9301	
	2 Hz	2.7247	0.9632	3 Hz
	2.5 Hz	2.5373	1.0650	
	3 Hz	2.2187	1.0338	2 Hz
Damping	100%	2.2960	1.1199	60%, 40%
	80%	2.4427	1.0625	
	60%	2.8267	1.0710	100%
	40%	2.8960	1.1702	100%
	20%	2.4613	1.2489	
Frequency	0 Hz	2.7387	1.1448	3 Hz
	1.5 Hz	2.6493	1.1886	3 Hz
	2 Hz	2.9267	1.1371	3 Hz
	2.5 Hz	2.5760	1.1766	3 Hz
	3 Hz	2.0320	0.9835	0, 1.5, 2, 2.5 Hz
Stiffness	100%	1.6507	0.9705	38%, 25%, 5%
	50%	2.0880	0.9791	38%, 25%, 5%
	38%	2.5547	1.0441	100%, 80%, 25%
	25%	3.0480	0.9978	100%, 80%, 38%, 5%
	5%	2.5840	1.1097	100%, 80%, 25%
Frequency	0 Hz	2.3200	1.1166	2 Hz
	1.5 Hz	2.3627	1.1386	2 Hz
	2 Hz	2.8320	1.2011	0, 1.5, 2.5, 3 Hz
	2.5 Hz	2.3467	1.0869	2 Hz
	3 Hz	2.0640	0.9791	2 Hz

TABLE 3.2 – Results of the test of main effects.

There is a significant difference between the frequencies of 2 Hz, which yields the best results, and 3 Hz. The frequencies of 1.5 Hz and 2.5 Hz are not statistically different from the other two.

The effects of the damping coefficient and the frequency were statistically significant, except for the interaction. There is no significant difference between a coefficient of 60% and 40%, which yields the best results, but 100% differs from them. 80% and 20% are not statistically different from the other values. There is a significant difference between the frequency of 3 Hz, which yields the worst results, and each of the other frequencies, which are not statistically different among themselves. The interaction effect is not significant, but not by a large margin compared to the other two pairs of parameters. This phenomenon can be easily explained. A

system with a sufficiently low damping coefficient overshoots while trying to stabilize to the reference position with the impedance controller, introducing noticeable transitory oscillations. This creates the illusion, from the user's point of view, of intended motion even when the reference trajectory is a fixed point, i.e., a 0 Hz frequency. For the same reason, at higher frequencies, a system with a weak damping coefficient becomes unstable, which is not natural for a handshake. Fig. 3.8b shows this behaviour for the lowest (0 Hz) and highest (3 Hz) frequencies studied.

The effects of the stiffness coefficient and the frequency were statistically significant, except for the interaction. There is a significant difference between the stiffness coefficients. The difference between the coefficients of 100% and 50% is not statistically significant, but it is relative to the other three. The same can be said about 38% and 5%. A 25% stiffness is different from each of the other values and yields the best results. There is also a significant difference between the frequency of 2 Hz, which yields the best results, and each of the other frequencies, which are not statistically different among themselves.

To summarize, a frequency of 2 Hz tends to yield better results against all three other parameters, but similar to 1.5 Hz and 2.5 Hz. A frequency of 3 Hz produces the worst results. The different amplitudes studied did not have an impact on the results. The damping coefficients of 60% and 40% produced a more natural handshake than the other coefficients, but similar to 80% and 20%. A stiffness coefficient of 25% is clearly more natural than the rest.

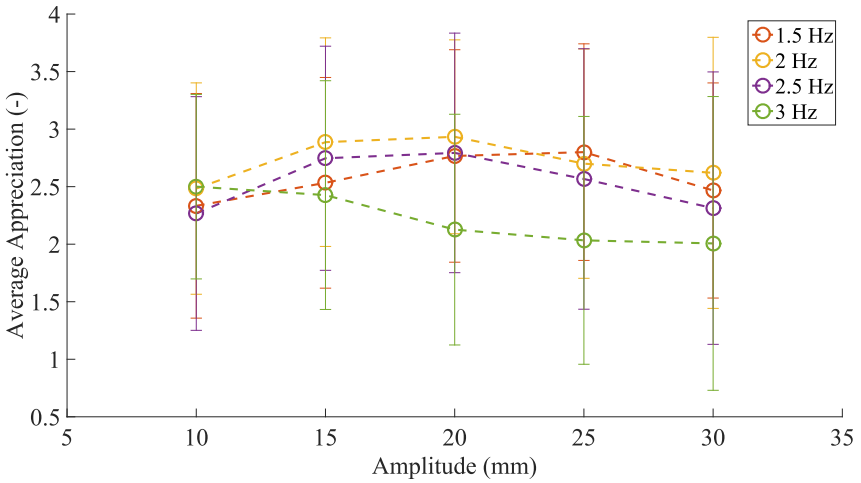

(a) Oscillation amplitude

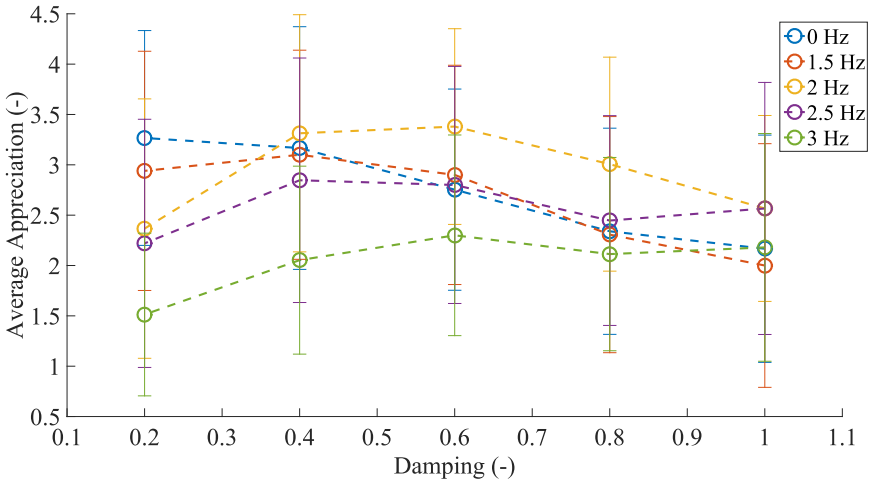

(b) Damping coefficient

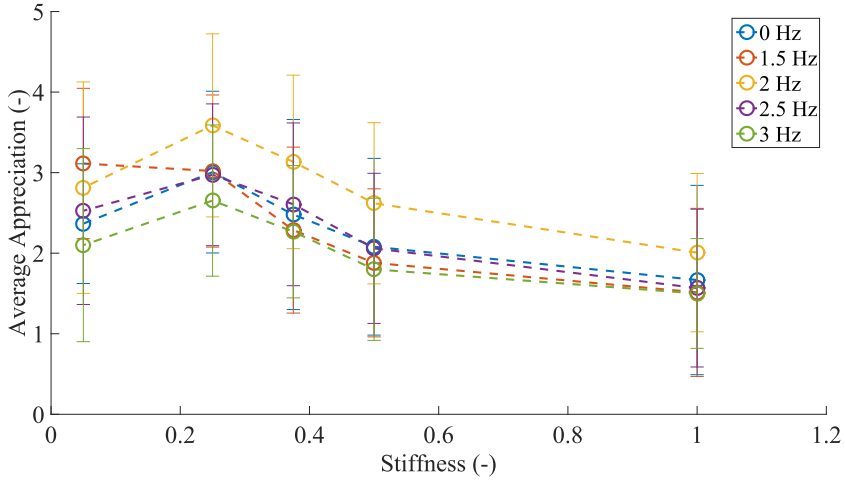

(c) Stiffness coefficient

FIGURE 3.8 – Average appreciation of a handshake based on the different parameters studied.

3.7.3 Observations

The experimentation conducted with the subjects allowed different aspects of the overall prototype to be observed.

As mentioned before, the reference trajectory begins in a downward direction. This fixed direction was not problematic for any of the subjects as none of them noticed it. When asked about it, they all needed to try the handshake again to answer.

The passive thumb was deemed insufficient to produce a very natural grasping effect but this limitation was not considered critical by the users. Regardless, the mechanical design could be improved to incorporate a better thumb actuation.

The palm behaviour, the reaction time and the grasping force and feeling were all considered realistic. The addition of a fourth finger would also improve the prototype. Some subjects also mentioned the improved realism that a skin-like glove could provide since the plastic fingers and palm did not feel natural to the touch.

Finally, some subjects mentioned the lack of adaptability in the prototype's behaviour, which was expected due to the absence of a feedback loop in the arm controller. Means of improving the prototype's adaptability, mainly the motion of the arm, is to be studied further. For instance, a force feedback loop could be implemented to estimate the human intention and adapt the robot's trajectory to harmonize the motion.

3.8 Multimedia Extension

A video accompanying this article shows the haptic robotic hand prototype mounted on a *Kuka LWR 4+* robot. The video demonstrates the features of the robotic hand and provides examples of human-robot handshakes performed with the prototype. The video is available at : `https://youtu.be/uy_HZAfqUUM`.

3.9 Conclusion and Future Work

This project's global objective is to emulate a realistic and natural handshake between a human and a robot. A first step toward this goal is presented in this paper. More specifically, a robotic hand designed to emulate a handshake is introduced. Using a compliant palm and underactuated fingers, this robotic hand uses a position-controlled feedback loop to produce a realistic grasping experience. Mounted on a serial manipulator using an impedance controller around a sinusoidal trajectory, this prototype is used to study the motion and behaviour of multiple handshakes. Experimentation was used to identify different values of the parameters of the estimated trajectory that are considered more natural, such as frequency, amplitude, and damping and stiffness coefficients. From the experiments, limitations of the prototype were

identified, as well as possible future improvements. For instance, the realism of the prototype would benefit from the addition of a fourth finger and a better thumb actuation. A skin-like glove would also help. The adaptability of the prototype's arm motion was found to be lacking, which was expected as it was not yet implemented. Future work includes the implementation of a feedback loop for the arm control, allowing the robot's intent to adapt to the user's and reach a certain synchronization, a harmony of motion.

Conclusion

> On paie mal un maître en ne restant toujours que l'élève.
>
> Friedrich Nietzsche, Ainsi parlait Zarathustra

Le but de la recherche présentée ici consiste à étudier et développer des interfaces haptiques capables de produire une interaction physique intuitive et naturelle entre un humain et un robot. Chacun des trois chapitres présentés dans cette thèse touche directement à l'interaction physique humain-robot. Ils convergent tous sans équivoque vers l'objectif général de par leur étude de différents aspects de l'architecture macro-mini.

Le Chapitre 1, l'étudiant a porté sur la traduction de l'information d'une interface en déplacement adéquat d'un robot. Plus particulièrement, différentes stratégies onr été étudiées pour résoudre le problème cinématique inverse dans le cadre de l'utilisation des coquilles à faible impédance à titre d'interface haptique. Ces coquilles passives sont montées sur des membrures du robot. Ce robot doit alors suivre les déplacements de ces coquilles lorsque l'utilisateur les manipule. Dans ce cas, le macro (le robot) est actif et le mini (les coquilles) est passif. Grâce à des simulations, un indice de performance a été développé pour comparer les différentes stratégies dans leur faculté à suivre le déplacement désiré par l'humain.

Ensuite, au Chapitre 2, des outils ont été développés pour analyser l'impact de l'échelle de l'interface sur la bande passante possible de l'interaction. L'architecture macro-mini est toujours considérée, où les deux mécanismes sont actifs dans le but de manipuler des charges lourdes (de l'ordre des 100 kg). Le robot mini est actif dans ce cas pour être en mesure d'appuyer l'utilisateur dans le déplacement de la lourde charge, ce qui n'est pas possible avec un mini passif. Il est cependant important, malgré que le mini soit actif, qu'il demeure rétrocommandable pour permettre le naturel de l'interaction. Différentes contraintes imposées aux déplacements de la charge sont considérées, *e.g.*, les normes de sécurité, les capacités cinématiques et dynamiques des deux mécanismes et autres. En fonction de ces contraintes, il a été possible de déterminer le débattement requis pour le mini mécanisme afin de permettre la bande passante désirée.

Enfin, au Chapitre 3, une interface haptique capable de produire une poignée de main réaliste

avec un utilisateur humain été développée et démontrée expérimentalement. Plus particulièrement, une main robotique a été conçue en s'inspirant de l'anatomie humaine. Cette main robotique est capable d'émuler la compression de la paume et la fermeture des doigts de manière naturelle lors d'une poignée de main. Un contrôle actif du bras a été ajouté à la main robotique pour permettre d'attribuer une personnalité au robot, en variant différents paramètres de la trajectoire générale, *i.e.*, l'amplitude, la fréquence ainsi que les coefficients d'amortissement et de raideur. La main robotique peut être considérée comme le robot mini et le bras, comme le robot macro. Des expérimentations auprès de sujets humains ont permis d'identifier les valeurs jugées plus naturelles de ces coefficients ainsi que des améliorations possibles à apporter au prototype dans le futur.

Futures avancées

Chacun des chapitres présentés dans cette thèse apporte de l'information importante quant à la conception d'interfaces haptiques pour l'interaction physique humain-robot. Ceci étant dit, il y a toujours place à l'amélioration et à la progression. Voici quelques pistes qui pourraient être suivies pour mener encore plus loin les recherches poursuivies dans cette thèse.

Pour ce qui est des coquilles à faible impédance, l'étape suivante consisterait à valider expérimentalement les simulations. Bien qu'elles soient intéressantes en elles-mêmes, de véritables données expérimentales aideraient à progresser, ne serait-ce que pour confirmer (ou même infirmer) les hypothèses posées. Également, différentes formes de coquilles pourraient être développées pour différentes applications. Plus encore, ce principe de coquilles à faible impédance pourrait être porté à différents types de robots. Il pourrait par exemple être utilisé sur des robots industriels pour les rendre plus collaboratifs.

Ensuite, l'analyse du robot mini actif dans le Chapitre 2 est faite en considérant des contraintes similaires, peu importe la fréquence visée. Il serait intéressé de définir différents régimes d'utilisation. Par exemple, à basse fréquence, une limite en vitesse de 1 m/s pour la charge représente presque une vitesse de marche normale. Dans une telle situation, si l'utilisateur se déplace physiquement (marche) en même temps que la charge, les demandes au macro pour suivre le mini seraient sans doute moindres qu'en considérant un véritable déplacement harmonique. Autrement, à plus haute fréquence, l'utilisateur serait en mesure de déplacer seulement ses bras et ses mains, limitant ainsi l'amplitude faisable autrement que seulement par la force qu'il est capable de produire. Ainsi, les différentes contraintes devraient être revues en fonction du régime d'utilisation, particulièrement les contraintes de sécurité, de vitesse et d'accélération. En plus de valider (ou infirmer) les simulations, l'expérimentation pourrait être intéressante pour identifier ces régimes ainsi que quantifier les différentes contraintes associées à chacun.

De plus, les résultats présentés dans le Chapitre 2 ont été obtenus en ne considérant qu'un seul degré de liberté pour le macro comme pour le mini. Une prochaine étape serait de poursuivre

l'analyse et l'expérimentation pour un système à plusieurs degrés de liberté, *e.g.*, un système SCARA à 4 degrés de liberté.

Enfin, pour l'interface destinée à la poignée de main, la prochaine étape consisterait à ajouter une boucle de rétroaction au contrôleur du bras. En effet, pour l'instant, bien que variable en fonction des différents paramètres, la trajectoire du bras est prédéfinie avant le premier contact. C'est-à-dire, la trajectoire ne s'adapte pas aux désirs de l'utilisateur. En d'autres mots, le robot macro ne réagit pas au robot mini. Il pourrait être qualifié d'intransigeant, si le coefficient de raideur est suffisamment élevé. Bien que l'intransigeance soit un trait de personnalité parfaitement humain, il est rare qu'une poignée de main ne soit pas influencée du tout par l'un des deux participants. Ajouter cette boucle de rétroaction ferait du prototype un véritable système macro-mini. Ensuite, pour améliorer le ressenti tactile du prototype, une peau pourrait être ajoutée, tout comme un quatrième doigt. Le pouce pourrait également être actionné.

Les interactions physiques humain-robot vont probablement prendre une place toujours grandissante dans le monde. Que ce soit en réadaptation ou pour assister les personnes âgées, dans le domaine médical ou militaire, pour l'exploration spatiale, dans l'industrie ou simplement à la maison, les robots vont faire leur entrée pour aider les humains et simplifier leur vie, où ce n'est pas déjà fait. Il sera donc primordial que les robots soient en mesure de partager une bande passante physique avec les humains. Il s'agit là du potentiel de l'approche macro-mini qui cherche à amener la bande passante des robots vers celle des humains. Il est facile d'imaginer l'utilité d'un tel système sur les chaînes de montage, où un travailleur serait en mesure de manipuler de lourdes charges tout en conservant toute sa dextérité manuelle. Et ce n'est là que la pointe de l'iceberg, ce futur imaginé peut être extrapolé à nombre de domaines différents où la dextérité humaine et la précision/répétabilité et la force des robots pourraient cohabiter.

Bibliographie

[1] P. D. Labrecque, J. Haché, M. Abdallah, and C. Gosselin. Low-impedance physical human-robot interaction using an active–passive dynamics decoupling. *IEEE Robotics and Automation Letters*, 1(2) :938–945, 2016.

[2] T. Laliberté and C. Gosselin. Low-impedance displacement sensors for intuitive physical human-robot interaction : motion guidance, design, and prototyping. In *IEEE Transactions on Robotics (to appear)*, 2021.

[3] P. D. Labrecque, T. Laliberté, S. Foucault, M. E. Abdallah, and C. Gosselin. uMan : A low-impedance manipulator for human–robot cooperation based on underactuated redundancy. *IEEE/ASME Transactions on Mechatronics*, 22(3) :1401–1411, 2017.

[4] T. S. Tadele, T. de Vries, and S. Stramigioli. The safety of domestic robotics : A survey of various safety-related publications. *IEEE Robotics Automation Magazine*, 21(3) :134–142, 2014.

[5] J. Krüger, T.K. Lien, and A. Verl. Cooperation of human and machines in assembly lines. *CIRP Annals*, 58(2) :628 – 646, 2009. ISSN 0007-8506. doi : https://doi.org/10.1016/j.cirp.2009.09.009. URL http://www.sciencedirect.com/science/article/pii/S0007850609001760.

[6] Andrea Cherubini, Robin Passama, André Crosnier, Antoine Lasnier, and Philippe Fraisse. Collaborative manufacturing with physical human–robot interaction. *Robotics and Computer-Integrated Manufacturing*, 40 :1 – 13, 2016. ISSN 0736-5845. doi : https://doi.org/10.1016/j.rcim.2015.12.007. URL http://www.sciencedirect.com/science/article/pii/S0736584515301769.

[7] Sami Haddadin, Alin Albu-Schäffer, and Gerd Hirzinger. Requirements for safe robots : Measurements, analysis and new insights. *The International Journal of Robotics Research*, 28(11-12) :1507–1527, 2009. doi : 10.1177/0278364909343970. URL https://doi.org/10.1177/0278364909343970.

[8] V. Duchaine and C. M. Gosselin. General model of human-robot cooperation using a novel velocity based variable impedance control. In *Second Joint EuroHaptics Conference*

and Symposium on Haptic Interfaces for Virtual Environment and Teleoperator Systems (WHC'07), pages 446–451, March 2007. doi : 10.1109/WHC.2007.59.

[9] A. Lecours, B. Mayer-St-Onge, and C. Gosselin. Variable admittance control of a four-degree-of-freedom intelligent assist device. In *2012 IEEE International Conference on Robotics and Automation*, pages 3903–3908, May 2012. doi : 10.1109/ICRA.2012.6224586.

[10] Pascal D. Labrecque and Clément Gosselin. Variable admittance for pHRI : From intuitive unilateral interaction to optimal bilateral force amplification. *Robotics and Computer-Integrated Manufacturing*, 52 :1 – 8, 2018. ISSN 0736-5845. doi : https://doi.org/10.1016/j.rcim.2018.01.005. URL http://www.sciencedirect.com/science/article/pii/S0736584516303441.

[11] V. Duchaine and C. Gosselin. Safe, stable and intuitive control for physical human-robot interaction. In *2009 IEEE International Conference on Robotics and Automation*, pages 3383–3388, May 2009. doi : 10.1109/ROBOT.2009.5152664.

[12] A. Sharon, N. Hogan, and D. E. Hardt. High bandwidth force regulation and inertia reduction using a macro/micro manipulator system. In *Proceedings. 1988 IEEE International Conference on Robotics and Automation*, pages 126–132 vol.1, 1988.

[13] O. Khatib. Augmented object and reduced effective inertia in robot systems. In *1988 American Control Conference*, pages 2140–2147, 1988.

[14] N. Badeau, C. Gosselin, S. Foucault, T. Laliberté, and M. E. Abdallah. Intuitive physical human-robot interaction : Using a passive parallel mechanism. *IEEE Robotics Automation Magazine*, 25(2) :28–38, 2018.

[15] Clement M. Gosselin, Mehdi Tale Masouleh, Vincent Duchaine, Pierre-Luc Richard, Simon Foucault, and Xianwen Kong. Parallel mechanisms of the multipteron family : Kinematic architectures and benchmarking. In *Proceedings 2007 IEEE International Conference on Robotics and Automation*, pages 555–560, 2007. doi : 10.1109/ROBOT.2007.363045.

[16] Zheng Ma, Hian-Hian See, Geok-Soon Hong, Marcelo H. Ang, Aun-Neow Poo, Wei Lin, Pey-Yuen Tao, and Joel S. Short. Control and modeling of an end-effector in a macro-mini manipulator system for industrial applications. In *2017 IEEE International Conference on Advanced Intelligent Mechatronics (AIM)*, pages 676–681, 2017. doi : 10.1109/AIM.2017.8014095.

[17] Jian Li, Yisheng Guan, Haowen Chen, Bing Wang, Tao Zhang, Xineng Liu, Jie Hong, Danwei Wang, and Hong Zhang. A high-bandwidth end-effector with active force control for robotic polishing. *IEEE Access*, 8 :169122–169135, 2020. doi : 10.1109/ACCESS.2020.3022930.

[18] G. Boucher, T. Laliberté, and C. Gosselin. A parallel low-impedance sensing approach for highly responsive physical human-robot interaction. In *2019 International Conference on Robotics and Automation (ICRA)*, pages 3754–3760, 2019.

[19] R. Penrose. A generalized inverse for matrices. *Mathematical Proceedings of the Cambridge Philosophical Society*, 51(3) :406–413, 1955. doi : 10.1017/S0305004100030401.

[20] C. W. Wampler. Manipulator inverse kinematic solutions based on vector formulations and damped least-squares methods. *IEEE Transactions on Systems, Man, and Cybernetics*, 16(1) :93–101, 1986.

[21] Yoshihiko Nakamura and Hideo Hanafusa. Inverse Kinematic Solutions With Singularity Robustness for Robot Manipulator Control. *Journal of Dynamic Systems, Measurement, and Control*, 108(3) :163–171, 09 1986. ISSN 0022-0434. doi : 10.1115/1.3143764. URL https://doi.org/10.1115/1.3143764.

[22] A. Balestrino, G. De Maria, and L. Sciavicco. Robust control of robotic manipulators. *Proceedings of the 9th IFAC World Congress*, 6, 07 1984. doi : 10.1016/S1474-6670(17) 61347-8.

[23] W. A. Wolovich and H. Elliott. A computational technique for inverse kinematics. In *The 23rd IEEE Conference on Decision and Control*, pages 1359–1363, 1984.

[24] G. H. Golub and C. Reinsch. Singular value decomposition and least squares solutions. *Numer. Math.*, 14(5) :403–420, April 1970. ISSN 0029-599X. doi : 10.1007/BF02163027. URL https://doi.org/10.1007/BF02163027.

[25] Samuel R. Buss and Jin-Su Kim. Selectively damped least squares for inverse kinematics. *Journal of Graphics Tools*, 10(3) :37–49, 2005. doi : 10.1080/2151237X.2005.10129202. URL https://doi.org/10.1080/2151237X.2005.10129202.

[26] Andrea Maria Zanchettin, Elizabeth Croft, Hao Ding, and Miao Li. Collaborative robots in the workplace [from the guest editors]. *IEEE Robotics Automation Magazine*, 25(2) : 16–17, 2018. doi : 10.1109/MRA.2018.2822083.

[27] Neville Hogan. Impedance control : An approach to manipulation : Part III—applications. *Journal of Dynamic Systems, Measurement, and Control*, 107(1) :17, 1985. doi : 10.1115/1.3140701. URL https://doi.org/10.1115%2F1.3140701.

[28] CM Gosselin and A Hadj-Messaoud. Automatic planning of smooth trajectories for pick-and-place operations. *ASME Journal of Mechanical Design*, pages 450–456, 1993.

[29] Luigi Biagiotti and Claudio Melchiorri. *Trajectory Planning for Automatic Machines and Robots*. Springer Publishing Company, Incorporated, 1st edition, 2008. ISBN 3540856285.

[30] L. Sciavicco, Bruno Siciliano, and B. Sciavicco. *Modelling and Control of Robot Manipulators*. Springer-Verlag, Berlin, Heidelberg, 2nd edition, 2000. ISBN 1852332212.

[31] Peter M. Hall and Dee Ann Spencer Hall. The handshake as interaction. *Semiotica*, 45 (3-4), 1983.

[32] Deborah Schiffrin. Handwork as ceremony : The case of the handshake. *Semiotica – Journal of International Association for Semiotic Studies*, 12, 1974.

[33] William F. Chaplin, Jeffrey B. Phillips, Jonathan D. Brown, Nancy R. Clanton, and Jennifer L. Stein. Handshaking, gender, personality, and first impressions. *Journal of personality and social psychology*, 79 :110–7, 08 2000. doi : 10.1037/0022-3514.79.1.110.

[34] A. Melnyk, P. Henaff, V. Khomenko, and V. Borysenko. Sensor network architecture to measure characteristics of a handshake between humans. In *2014 IEEE 34th International Scientific Conference on Electronics and Nanotechnology (ELNANO)*, pages 264–268, April 2014. doi : 10.1109/ELNANO.2014.6873983.

[35] G. Tagne, P. Hénaff, and N. Gregori. Measurement and analysis of physical parameters of the handshake between two persons according to simple social contexts. In *2016 IEEE/RSJ International Conference on Intelligent Robots and Systems (IROS)*, pages 674–679, Oct 2016. doi : 10.1109/IROS.2016.7759125.

[36] Nicoló Pedemonte, Thierry Laliberté, and Clément Gosselin. Design, control and experimental validation of harri, a handshaking anthropomorphic reactive robotic interface. *Journal of Mechanisms and Robotics*, 8, 07 2015. doi : 10.1115/1.4031167.

[37] M. Arns, T. Laliberté, and C. Gosselin. Design, control and experimental validation of a haptic robotic hand performing human-robot handshake with human-like agility. In *2017 IEEE/RSJ International Conference on Intelligent Robots and Systems (IROS)*, pages 4626–4633, Sep. 2017. doi : 10.1109/IROS.2017.8206333.

[38] T. Kasuga and M. Hashimoto. Human-robot handshaking using neural oscillators. In *Proceedings of the 2005 IEEE International Conference on Robotics and Automation*, pages 3802–3807, April 2005. doi : 10.1109/ROBOT.2005.1570700.

[39] Tae Sato, Minoru Hashimoto, and Mina Tsukahara. Synchronization based control using online design of dynamics and its application to human-robot interaction. In *2007 IEEE International Conference on Robotics and Biomimetics (ROBIO)*, pages 652–657, Dec 2007. doi : 10.1109/ROBIO.2007.4522239.

[40] Guanghui Xie, Mina Jin, Deming Wu, and M. Hashimoto. Control for physical human-robot interaction based on online update of dynamics. In *2011 IEEE International Conference on Computer Science and Automation Engineering*, volume 2, pages 280–284, June 2011. doi : 10.1109/CSAE.2011.5952470.

[41] M. Jindai and T. Watanabe. A handshake robot system based on a shake-motion leading model. In *2008 IEEE/RSJ International Conference on Intelligent Robots and Systems*, pages 3330–3335, Sep. 2008. doi : 10.1109/IROS.2008.4650621.

[42] Yoshihide Yamato, Mitsuru Jindai, and Tomio Watanabe. Development of a shake-motion leading model for human-robot handshaking. In *2008 SICE Annual Conference*, pages 502–507, Aug 2008. doi : 10.1109/SICE.2008.4654707.

[43] Z. Wang, A. Peer, and M. Buss. An hmm approach to realistic haptic human-robot interaction. In *World Haptics 2009 - Third Joint EuroHaptics conference and Symposium on Haptic Interfaces for Virtual Environment and Teleoperator Systems*, pages 374–379, March 2009. doi : 10.1109/WHC.2009.4810835.

[44] Amir Karniel, Ilana Nisky, Guy Avraham, Bat-Chen Peles, and Shelly Levy-Tzedek. A turing-like handshake test for motor intelligence. In Astrid M. L. Kappers, Jan B. F. van Erp, Wouter M. Bergmann Tiest, and Frans C. T. van der Helm, editors, *Haptics : Generating and Perceiving Tangible Sensations*, pages 197–204, Berlin, Heidelberg, 2010. Springer Berlin Heidelberg. ISBN 978-3-642-14064-8.

[45] G. Avraham, I. Nisky, H. L. Fernandes, D. E. Acuna, K. P. Kording, G. E. Loeb, and A. Karniel. Toward perceiving robots as humans : Three handshake models face the turing-like handshake test. *IEEE Transactions on Haptics*, 5(3) :196–207, Third 2012. ISSN 1939-1412. doi : 10.1109/TOH.2012.16.

[46] I. Nisky, G. Avraham, and A. Karniel. Three alternatives to measure the human-likeness of a handshake model in a turing-like test. *Presence*, 21(2) :156–182, May 2012. ISSN 1054-7460. doi : 10.1162/PRES_a_00097.

[47] N. Pedemonte, T. Laliberté, and C. Gosselin. A bidirectional haptic device for the training and assessment of handwriting capabilities. In *2013 World Haptics Conference (WHC)*, pages 599–604, April 2013. doi : 10.1109/WHC.2013.6548476.

[48] H. Hashimoto and S. Manoratkul. Tele-handshake through the internet. In *Proceedings 5th IEEE International Workshop on Robot and Human Communication. RO-MAN'96 TSUKUBA*, pages 90–95, Nov 1996. doi : 10.1109/ROMAN.1996.568767.

[49] Nicolò Pedemonte, Thierry Laliberté, and Clément Gosselin. A haptic bilateral system for the remote human-human handshake. *Journal of Dynamic Systems, Measurement, and Control*, 139, 11 2016. doi : 10.1115/1.4035171.

[50] Henry Gray and Warren H Lewis. *Anatomy of the human body.* Philadelphia, Lea & Febiger, 1918. URL https://www.biodiversitylibrary.org/item/60234.